university of groningen / faculty of science and engineering

# Characterization & Optimization of Phase Camera for Advanced Virgo Gravitational Wave Detectors

## Master Thesis

by

Author: Yashwant Sing Bothra

to obtain the degree of

**Master of Science**
in Mechanical Engineering
Advanced Instrumentation track

| | | |
|---|---|---|
| Faculty: | Faculty of Science & Engineering, RUG | |
| Project Duration | Sep, 2023 - May, 2024 | |
| Thesis Committee: | dr. ing. M. G. van Beuzekom | Nikhef, principal supervisor |
| | dr. M. Kavatsyuk | RUG, principal supervisor |
| | dr. ir. G. de Lange | RUG, secondary supervisor |
| | dr. M. Tacca | Nikhef, supervisor |
| | dr. P. Kuijer | Nikhef, supervisor |

Nikhef

# Abstract

Gravitational wave (GW) detectors like Advanced Virgo (AdV) employ sensitive laser interferometric techniques to detect minute distortions in spacetime. However, instabilities such as misalignments, thermal lensing, and other optical aberrations can induce higher-order modes (HOMs) that compromise interferometer sensitivity and control. A thermal compensation system (TCS) has been commissioned in AdV, using phase cameras (PCs) as wavefront sensors to identify the mode content of the beam and correct for these aberrations. The PCs can image the spatial profiles for the carrier and all phase-modulated sidebands. However, due to the challenges in the interpretation of the phase images and its phase resolving capabilities, the practical use of the PC has been limited. This research focuses on optimizing the prototype PC setup developed at Nikhef, primarily aiming to improve the system's phase resolution.

In this research, we have characterized and optimized the prototype PC setup. We perform relative phase measurements of the heterodyne beat signal at 80 MHz. To improve the phase resolution, we conducted various stability measurements — vibrational, acoustic, and seismic — using different techniques and devices such as accelerometers, quadrant photodiodes, microphones, and geophones. These techniques were employed to identify the sources of high-frequency phase noise that lead to poor phase resolution and consequently fluctuations in the phase measurements.

The main sources of phase noise were identified primarily as vibrational and acoustic. All optical components of the setup resonate (or vibrate) at distinct frequencies. By identifying and mitigating some of these major noise sources, we improved the phase resolution of the setup to about 5.2 mrad ($\lambda$/1200 at $\lambda$ = 1064 nm), corresponding to an optical path length difference of 0.89 nm. The primary sources of phase noise in the current measurements are attributed to optical resonances of the mounts, observed in the 200-700 Hz frequency range. If these vibrational effects were minimized, the phase resolution of the setup could potentially be improved to 0.5 mrad or lower.

The results indicate that the prototype PC setup is highly stable and effectively designed, with phase-resolving capabilities well within the requirements. Further improvements in resolution could be achieved by more effectively isolating vibrational and acoustic disturbances from the interferometer.

# Nomenclature

## Abbreviations

| Abbreviation | Definition |
|---|---|
| ADC | Analog-to-digital converter |
| AdV | Advanced Virgo |
| ASD | Amplitude spectral density |
| CCD | Charged-coupled device |
| DAQ | Data acquisition |
| D.O.F | Degree of freedom |
| EM | Electromagnetic |
| FPGA | Field programmable gate array |
| GW | Gravitational wave |
| HG | Hermite-Gaussian |
| HOM | Higher order modes |
| LIGO | Laser Interferometer Gravitational-wave Observatory |
| Nikhef | National Institute for Subatomic Physics |
| OPL | Optical path length |
| OPD | Optical path length difference |
| PC | Phase camera |
| PDE | Partial differential equation |
| PM | Phase modulation |
| PSD | Power spectral density |
| QPD | Quadrant photodiode |
| RF | Radio-frequency |
| RMS | Root-mean square |
| RoC | Radius of curvature |
| TEM | Transverse electromagnetic modes |
| TCS | Thermal compensation system |

# Contents

**Abstract** i

**Nomenclature** ii

**1 Introduction** 1

**2 Lasers & Higher Order Modes** 3
2.1 Fundamental Principles in Optics . . . 3
2.2 Gaussian Mode . . . 4
2.2.1 Beam Properties . . . 5
2.2.2 Transmission of Gaussian Beams . . . 7
2.3 Higher Order Modes . . . 9
2.3.1 Hermite-Gaussian Modes . . . 9
2.4 Stigmatic & Astigmatic Beams . . . 9

**3 Phase Camera** 13
3.1 Working Principle of the Phase Camera . . . 14
3.2 Optical Setup of the Phase Camera . . . 14
3.2.1 Formulation . . . 16
3.2.2 Data Acquisition and Digital Demodulation . . . 17

**4 Phase Camera Setup Characterization** 19
4.1 Beam Profiling . . . 19
4.1.1 Reference Beam Characterization . . . 20
4.1.2 Test beam Characterization . . . 26
4.1.3 Discussion . . . 29

**5 Phase Measurements** 30
5.1 Phase Noise . . . 32
5.1.1 Error Sources . . . 33
5.1.2 Coupling . . . 33
5.2 Investigation of Phase Noise . . . 35
5.2.1 Vibrational Stability of the Setup . . . 37
5.2.2 Acoustic Noise . . . 43
5.2.3 Laser Stability Measurements . . . 43
5.3 Phase Resolution . . . 49
5.3.1 Comparison with Previous Measurements . . . 52

**6 Summary & Conclusion** 53
6.1 Future Work . . . 54

**Bibliography** 55

# 1

# Introduction

Albert Einstein's general theory of relativity defines gravity not as a mere force but as a geometric property of spacetime — a concept that predicted the existence of gravitational waves (GWs). These were first observed in 2015 by the Laser Interferometer Gravitational-wave Observatory (LIGO) detectors in the United States. Historically, scientists have relied almost exclusively on electromagnetic (EM) radiation (visible light, infrared, radio waves, etc.) to study the universe [1]. The observation of GWs has opened a new window in astronomy, enabling the study of black holes, neutron stars, among others [2].

GWs are defined as transverse quadrupole waves that travel at the speed of light and manifest as distortions in spacetime [3]. Imagine two freely falling test masses in space; as a GW passes, it alters the fabric of spacetime, changing the distance between these masses. This principle forms the basis of GW detectors, which use interferometric principles to measure minute changes in distance between suspended mirrors acting as test masses. It's truly astonishing how minute these changes are. The extent of this length change is quantified by the strain, h(t) = $\Delta$L/L , of the GW amplitude, where $\Delta L$ represents the change in the initial length L between the test masses. For the strongest GWs, the strain is in the order of $10^{-21}$. Thus, for a length L of 4 km, as is the case with LIGO detectors, the measured $\Delta L$ is in the order of $10^{-18}$ m. Therefore, the length changes produced by GWs are extremely small, making their detection exceptionally challenging.

GW detectors like LIGO and Advanced Virgo (AdV) operate based on the principles of a Michelson interferometer. An interferometer is a highly sensitive and precise optical system capable of measuring small distances or changes in distances, on the scale of fractions of a wavelength of light. This high sensitivity enables the detection of GWs. The principle of operation is straightforward: a laser beam, split into two by a beam splitter, travels along two perpendicular arms of equal length. Mirrors at the ends of these arms reflect the beams back to the beam splitter, where they recombine and interfere. GW detectors are designed such that under ideal conditions, the beams recombine destructively, producing no output at the detector port, known as the dark-port. However, when a GW passes through, it alters the length of one or both arms, changing the path lengths traveled by the beams. In this scenario, when the beams recombine, the interference is not completely destructive and leads to a measurable signal at the dark-port. This explanation provides a general overview of the working principle; the actual experimental setup involves an intricate optical design and control systems to ensure accurate measurement of GW signals.

To be able to measure these weak GW signals, the precision required for stability, mirror positioning, angular alignment, among others, is exceptionally high. Instabilities in the form of misalignments, mirror surface and substrate inhomogeneities, thermal lensing effects, and other optical aberrations can lead to higher-order modes (HOMs) resonating in the interferometer. HOMs disrupt the alignment control and reduce the sensitivity of the detectors [2, 4]. Ideally, only the fundamental Gaussian mode should resonate in these systems. To control and monitor the operational state of these systems and mode content of the beam, various sensors and techniques are employed: quadrant photodiodes (QPDs), Hartmann wavefront sensors, charged-coupled device (CCD) cameras, among others. These control

techniques, provide insight about the state of the interferometer, such that it can be kept in a condition suitable to observe GWs [4]. The phase camera (PC) is one such sensor (technique) deployed in AdV to monitor the mode content of the output beam from the interferometer.

In the case of AdV, the power of the laser beams is increased to improve the sensitivity of the detector. The increase in laser power induces thermal aberrations and HOMs easily resonate in the interferometer [5, 6]. In order to tackle this problem, a thermal compensation system (TCS) has been developed and commissioned in AdV. The PC is employed in the TCS as a wavefront sensor to study and monitor the real-time status of the beam and determine its mode content. These cameras can separately (independently) measure the amplitude, phase, and spatial modes of the carrier and phase-modulated (PM) sidebands exiting the GW interferometer. PM sidebands are important for maintaining the cavities at the desired resonance, and probing these sidebands is necessary for controlling the interferometer's state. The scientific goal of the PC is to study the HOMs of the output beam from the interferometer and subsequently correct for any optical aberrations present within the system.

The PC was first tested in AdV, revealing the need for better sensitivity and phase resolution capabilities. To address this, a prototype PC was developed at Nikhef to investigate the requirements of AdV [4]. Although the intended use of PC is very broad and multi-purpose, this research represents a step forward to understanding the setup and the PC better. In this work, we characterize and optimize the PC setup in Nikhef. Our interest primarily lies in studying the short-time scale drifts (fluctuations) observed in the phase measurements of the laser beam wavefronts, which attributes to the phase resolution of our system. Our overall goal is to improve the phase resolution of the setup. To achieve this, we have conducted various stability measurements using different techniques and devices, including accelerometers, QPDs, microphones, and geophones. These were employed to identify the sources of phase noise and drifts that affect the phase resolution. Efforts were then made to mitigate these identified disturbances.

The structure of this thesis is as follows: Chapter 2 lays the groundwork by introducing basic principles related to Gaussian beams and HOMs. Chapter 3 then delves into the working principles and the prototype optical setup of the PC. In Chapter 4, we characterize the PC setup. In Chapter 5, we extensively discuss phase measurements and investigate various phase noise sources within our setup. The latter part of this chapter systematically demonstrates the improvements in the measured phase resolution. Finally, Chapter 6 summarizes the thesis, presents conclusions, and outlines potential topics for future research.

# 2

# Lasers & Higher Order Modes

The phase camera setup is a sophisticated optical system specifically designed for capturing and measuring laser beam wavefronts. Our primary focus is on determining the amplitude and phase distribution of these optical wavefronts. To comprehend its design and operation, a grasp of key concepts related to lasers and its optical nature is important. This chapter focuses on explaining the characteristic properties of laser beams. Our focus lies in understanding the different modes and behavior of laser (or Gaussian) beams as they traverse through various optical components. This chapter lays the foundation for the work presented in this thesis. Unless stated otherwise the chapter is based on references [7, 8, 9, 10].

## 2.1. Fundamental Principles in Optics

The primary theories for understanding light and optical phenomena are geometrical (or ray) and wave optics. Geometrical optics simplifies light into rays, while wave optics provides a more fundamental and comprehensive explanation, focusing on amplitude, phase, and wavefront information of light. In the context of the PC, we aim to measure these exact properties of a laser beam. Therefore, we adopt the wave theory approach to understand the laser beams.

Central to the theoretical underpinnings of the wave theory and study of light's properties are the Maxwell's equations. Maxwell's equations allow for the derivation of the wave equation.

$$\boxed{\nabla^2\Psi(r,t) = \frac{1}{c^2}\frac{\partial^2\Psi(r,t)}{\partial t^2}} \tag{2.1}$$

Equation 2.1 serves as the wave equation in vacuum. It uses a generalized notation to define any wave phenomena, including electromagnetic waves. Any wave phenomenon can be mathematically described by a real function of space $r = (x, y, z)$ and time $t$, typically represented as $\Psi(r, t)$ and referred to as the wave function. Integral to this equation is speed at which the waveform or disturbance propagates through space and time. In vacuum this is equivalent to the speed of light, $\mathbf{c} = 2.9979 \times 10^8$ m/s.

The wave equation is essentially a partial differential equation (PDE). This PDE can possess numerous solutions, and given its linearity, any combination of these solutions can be added together to generate other valid solutions—a concept known as the superposition principle. Our primary goal is to identify functions $\Psi(r, t)$ that not only satisfy the PDE but also encapsulates the nature of light emitted by lasers. Prior to exploring these solutions to the wave equation, we will introduce certain approximations to streamline our analytical description.

To simplify our mathematical analysis and calculations, we will represent the real wavefunction in complex notation and we will utilize a mathematical technique - separation of variables - to represent the general wave function as a product of separate spatial and temporal components:

$$\Psi(r,t) = \psi(r)e^{-i2\pi\nu t}. \tag{2.2}$$

In this formulation, $\psi(r) = A(r)e^{i\varphi(r)}$ represents the time-independent or spatial component, commonly referred to as the complex amplitude of the wave function, $\nu$ denotes the temporal frequency of the wave, and the term $e^{-i2\pi\nu t}$ captures the time-varying aspect of the wave. The physical field is the real part of the complex field $\Re\{\Psi(r,t)\}$. Substituting this complex representation into the wave equation 2.1, leads to a differential equation for the complex amplitude $\psi(r)$, which is known as the Helmholtz equation.

$$\boxed{\nabla^2\psi(r) + k^2\psi(r) = 0} \tag{2.3}$$

Here k represents the wave number, which is related to the wavelength ($\lambda$) or frequency of the wave by k = $2\pi/\lambda$ = $2\pi\nu/c$. The Helmholtz equation addresses only the spatial variation of a wave function oscillating harmonically in time.

Building on the Helmholtz equation, now assume a solution of the form $\psi(r) = A(r)e^{-ikz}$ which is a plane wave, propagating along the z-axis, and modulated transversely by the complex envelope A(r). By substituting this solution $\psi(r)$ to the Helmholtz equation, we arrive at:

$$\left(\frac{\partial^2 A}{\partial x^2} + \frac{\partial^2 A}{\partial y^2} + \frac{\partial^2 A}{\partial z^2} - 2ik\frac{\partial A}{\partial z}\right) \cdot e^{-ikz} = 0. \tag{2.4}$$

To further simplify the equation we make a paraxial approximation. This approximation proves remarkably effective for laser beams. A wave is termed paraxial when its propagation direction is nearly parallel to a defined optical axis. More formally, a paraxial wave satisfies the condition that its angle of propagation ($\theta$) with respect to the optical axis is small, that is, $\sin\theta \simeq \theta$. Laser beams are well-collimated and have small angular distribution, thus falling under the regime of the paraxial approximation. Under the paraxial approximation, we assume the modulation A(r) is a slowly varying function of the z-axis (optical axis), such that $\frac{\partial^2 A}{\partial z^2} << 2ik\frac{\partial A}{\partial z}$. Incorporating this into the equation 2.4 leads us to the paraxial Helmholtz equation:

$$\boxed{\nabla_T^2 A(r) - 2ik\frac{\partial A(r)}{\partial z} = 0} \tag{2.5}$$

where $\nabla_T^2 = \partial^2/\partial x^2 + \partial^2/\partial y^2$ is the transverse Laplacian operator. The paraxial approximation also directly leads to the concept of transverse electromagnetic (TEM) waves or modes. TEM waves are characterized by their electric and magnetic fields being perpendicular (transverse) to the direction of wave propagation, embodying the essence of paraxial waves.

Having introduced the paraxial Helmholtz equation, we now turn our attention to the solutions that satisfy this equation. One solution of particular interest, especially in the context of laser beams, is the Gaussian mode.

## 2.2. Gaussian Mode

The most fundamental solution of the paraxial wave equation is the Gaussian mode or $TEM_{00}$ mode. At this point, it will be nice to stress on the word ”fundamental” and mention that, it is not the only solution to the paraxial wave equation, as we will see in the later parts of this chapter. The mathematical description of Gaussian mode leads to a spatially confined and nondiverging beam - which represents the quality of laser beams. In this section we will define few characteristic parameters and transformation of the Gaussian beams.

The concept and representation of paraxial waves was introduced in section 2.1. In order for the complex amplitude $\psi(r)$ to satisfy the Helmholtz equation, the complex envelope $A(r)$ must satisfy the paraxial Helmholtz equation. One such solution for the complex envelope $A(r)$ is given by,

$$A(r) = \frac{A_o}{q(z)}\,\mathsf{exp}\left[-ik\frac{x^2+y^2}{2q(z)}\right], \quad q(z) = z + iz_R. \tag{2.6}$$

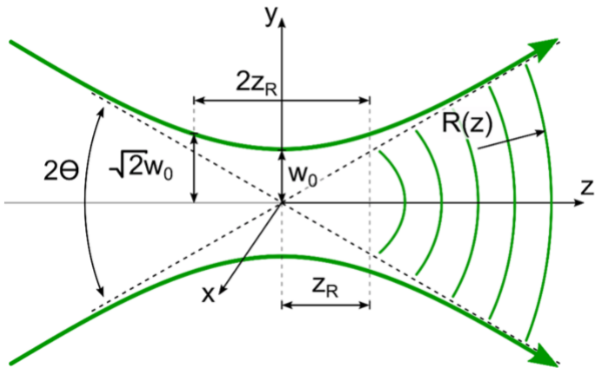


**Figure 2.1:** Evolution of the Gaussian beam size (radius) along the propagation axis [11].

The quantity $q(z)$ is called the complex beam parameter of the beam and has to be imaginary to be able to satisfy the paraxial equation. It is defined using the real parameter $z_R$, which is known as the Rayleigh range. The q-parameter can be expressed in terms of its real and imaginary parts by defining two real functions - width w(z) and and wavefront radius of curvature R(z) such that:

$$\frac{1}{q(z)} = \frac{1}{R(z)} - i\frac{\lambda}{\pi w^2(z)} \tag{2.7}$$

Substituting the q-parameter representation shown in equation 2.7 in equation 2.6, leads directly to the expression for the complex amplitude $\psi(r)$ of the Gaussian beam:

$$\boxed{\psi(r) = A_1 \frac{w_o}{w(z)} \exp\left[-\frac{x^2+y^2}{w^2(z)}\right] \exp\left[-ikz - ik\frac{x^2+y^2}{2R(z)} + i\tan^{-1}\left(\frac{z}{z_R}\right)\right]} \tag{2.8}$$

$$w(z) = w_0\sqrt{1+\left(\frac{z}{z_R}\right)^2} \tag{2.9}$$

$$R(z) = z\left[1+\left(\frac{z_R}{z}\right)^2\right] \tag{2.10}$$

$$\xi(z) = \tan^{-1}\left(\frac{z}{z_R}\right). \tag{2.11}$$

In the Gaussian beam expression we have defined $A_1 = A_o/iz_R$. Each of these beam properties, as expressed in equations 2.9 to 2.11, will be further elaborated upon.

### 2.2.1. Beam Properties

#### Beam Radius/Width

The beam width or radius, w(z), of a Gaussian beam is a parameter describing the transverse extent of the beam spot, and is defined as the radial distance from the beam's axis to where its intensity falls to $1/e^2$ (approximately 13.5%) of its peak intensity. The beam's narrowest point, known as the beam waist, is represented by $w_o$. The evolution of beam width for a Gaussian beam along the propagation axis (z) is shown in figure 2.1 and is described by the following mathematical relationship:

$$w(z) = w_o\sqrt{1+\left(\frac{z}{z_R}\right)^2}.$$

The spot size of the beam at any transversal plane is equal to 2w(z). The Rayleigh length, $z_R$, is defined by the condition that the beam width at $z_R$ is $\sqrt{2}w_o$, indicating a doubling of the area of the beam's cross-section.

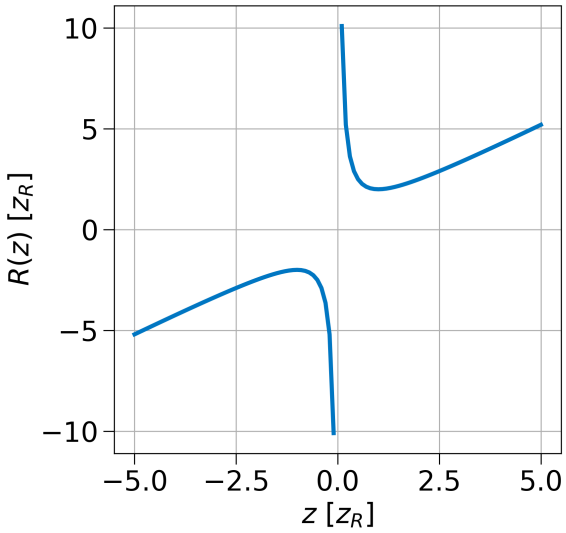


**Figure 2.2:** Evolution of the RoC of a Gaussian beam wavefront.

### Beam Divergence

Beam divergence characterizes the angular spread of a beam as it propagates along the optical axis. According to equation 2.9, in the regime where z » $z_R$, the initial term can be neglected, simplifying the expression to:

$$w(z) \simeq \frac{w_o}{z_R} z = \Theta z.$$

Here, beam divergence $\Theta$ is defined as:

$$\Theta = \frac{w_o}{z_R} = \frac{\lambda}{\pi w_o}.$$

As depicted in figure 2.1, the angle $2\Theta$, signifies twice the beam's divergence angle.

### Wavefronts

The other component of the complex beam parameters is R(z) - radius of curvature (RoC) of the laser beam wavefront.

$$R(z) = z\left[1 + \left(\frac{z_R}{z}\right)^2\right]. \tag{2.12}$$

A plot showing the evolution of the radius of curvature as a function of z is shown in figure 2.2. As illustrated in the figure at z=0, R(z) is infinite meaning that the wavefronts are planar. At $z = z_R$, the beam has the minimum radius i.e. maximum curvature. After the Rayleigh length the wavefronts of the beam are approximately similar as those of a spherical wave. The wavefronts of a Gaussian beam transition from being planar at z=0 to again becoming planar as z approaches infinity. Within this range, the beam transforms, adopting a spherical wavefront as it propagates through the z-domain.

### Phase

The phase term of the Gaussian beam as given by the equation 2.8 is,

$$\varphi(x, y, z) = kz + k\frac{x^2 + y^2}{2R(z)} - \tan^{-1}\left(\frac{z}{z_R}\right).$$

The first term, kz, represents the linear phase variation along the optical axis, similar to the phase accumulated by the wavefronts of a plane wave. The second term in the equation represents the quadratic phase variation in the transverse plane (x-y plane). As the beam propagates, the curvature

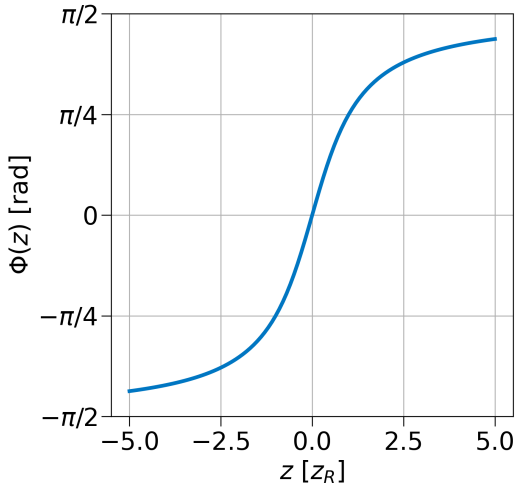


**Figure 2.3:** Evolution of the Gouy phase for a Gaussian beam along the propagation axis.

of the wavefronts changes, leading to a corresponding change in the phase distribution across the beam profile. The third term is the Gouy phase. It is the extra longitudinal phase lag originating from the slower phase velocity of a Gaussian beam compared to a plane wave. The variation of Gouy phase along the propagation axis is shown in figure 2.3.

### Intensity

The optical intensity of a Gaussian beam is a function of both the transversal and longitudinal positions, defined as $I(r) = |\psi(r)|^2$.

$$I(r) = I_o \left[\frac{w_o}{w(z)}\right]^2 \exp\left[-2\frac{x^2+y^2}{w^2(z)}\right]. \tag{2.13}$$

In the above equation $I_o = |A_1|^2$. Both the intensity and amplitude distribution of a laser beam are Gaussian, and the width of this distribution is determined by the beam size. This beam size changes along the propagation axis of the beam, which in turn changes the width of the distribution and the peak optical intensity. Figure 2.4 illustrates the amplitude and intensity of the Gaussian beam as functions of the radial distance in the $x$ direction, plotted for different beam sizes, $w_0$, $2w_0$, and $3w_0$. This highlights how the intensity distribution of the beam evolves with increasing beam size.

## 2.2.2. Transmission of Gaussian Beams

Within the paraxial approximation, an optical system can be fully described by a $2 \times 2$ ray transfer matrix. This framework allows us to define a paraxial optical system using four parameters - A, B, C, and D - which correspond to the elements of the matrix. The numerical value of these elements depends on the optical components (lens, mirror, etc.) and its parameters (focal length, etc.). This matrix relates the position (height) and inclination with respect to the optical axis of the transmitted ray to the incident ray. The transfer matrix, also known as the ABCD law, enables us to predict the properties of the transmitted beam. Figure 2.5 illustrates the essence of using matrix representation for an optical system. The mathematical relationship between the q-parameters of beams at the input ($q_1$) and output ($q_2$) planes of a paraxial optical system is given by the equation:

$$q_2 = \frac{Aq_1 + B}{Cq_1 + D}. \tag{2.14}$$

By expressing the q-parameter of the beam as a function of w(z) and R(z), as shown in equation 2.7, we can establish the relationship between these functions for the incident and transmitted beams.

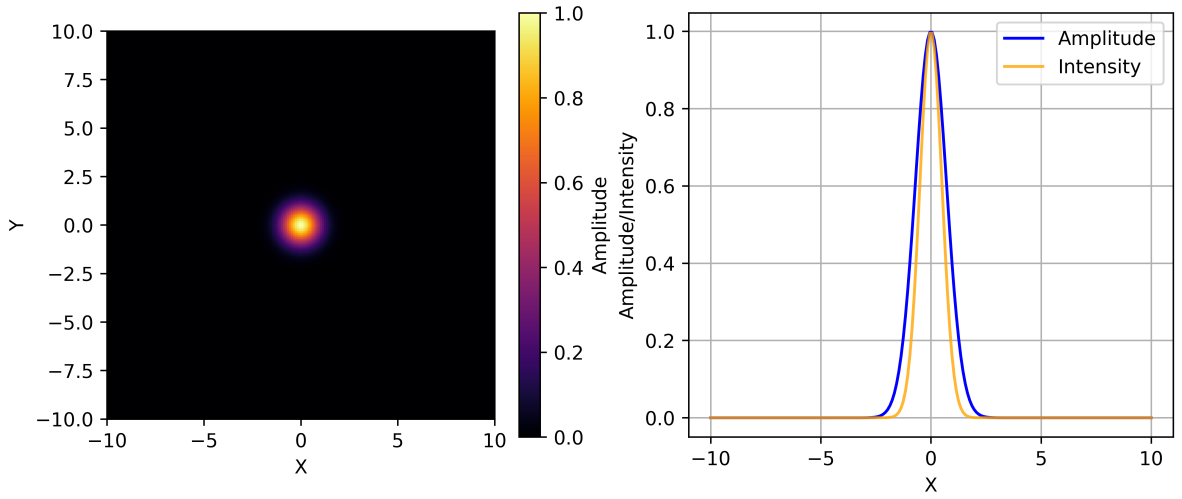


**(a)** Beam size $w_o$

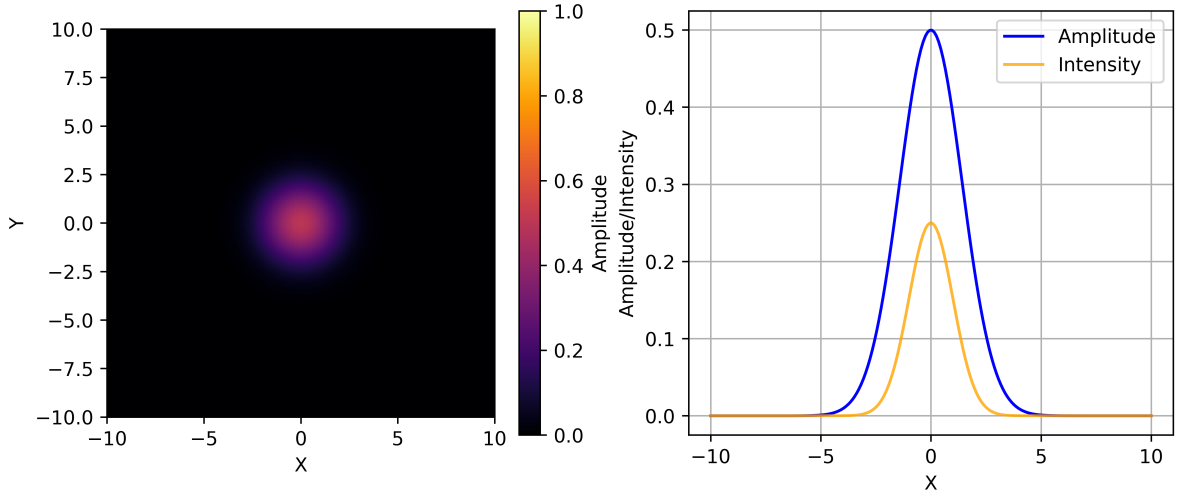


**(b)** Beam size $2w_o$

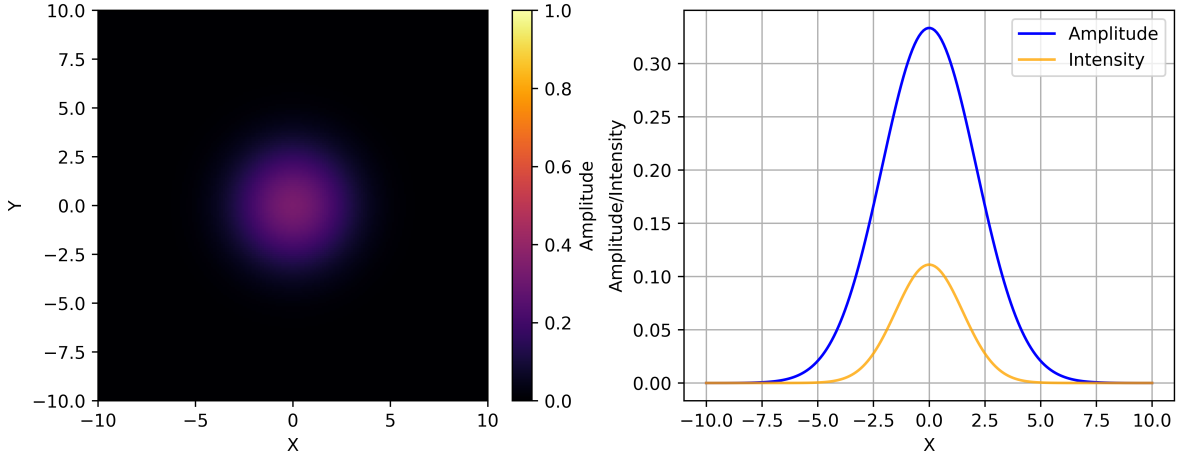


**(c)** Beam size $3w_o$

**Figure 2.4:** Normalized intensity and amplitude distribution of a Gaussian beam at a wavelength of 1064 nm, comparing the distribution across three different beam sizes along the propagation axis.

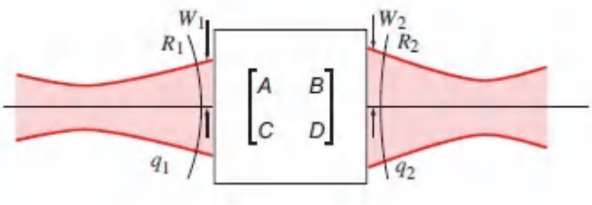


**Figure 2.5:** Transmission of a Gaussian beam through an arbitrary paraxial optical system defined by an ABCD matrix [8]

## 2.3. Higher Order Modes

The Gaussian mode, or the fundamental $TEM_{00}$, represents the lowest-order solution to the paraxial approximation of the Helmholtz equation. It is distinguished by its single beam spot, symmetric intensity profile that diminishes in all directions away from the beam center. There are other solutions as well exhibiting more complex geometries and amplitude distributions in the transversal plane, correspondingly leading to a more obscure mathematical description. These solutions are often referred to as higher order modes (HOMs). In this section we will briefly introduce the Hermite-Gaussian (HG) mode.

You may wonder to why this construct is necessary and relevant for this thesis. Well, the PC for AdV is used to detect HOMs present in the laser beam and use the TCS to correct for them. These HOMs are unwanted and in ideal conditions we would want only the fundamental mode resonating in the cavities and optical systems. The prototype setup of the PC, don't have these HOMs resonating in the setup but to explain you the global picture of the PC, this construct is necessary. Hence we will define these concepts sufficiently enough, so that the overall functionality and use of PC is well understood.

### 2.3.1. Hermite-Gaussian Modes

Higher-order beam solutions can be found by solving the paraxial Helmholtz equation. One family of the resulting solutions is named as HG beams, or $TEM_{lm}$. The HG mode is distinguished by their unique spatial distributions, which can exhibit multiple peaks and nodes along both the horizontal and vertical axes. Such modes exhibit non-Gaussian amplitude distributions but share the wavefronts of the Gaussian beam. The complex field amplitude for HG modes can be defined by:

$$\psi_{l,m}(r) = A_{l,m}\left[\frac{w_0}{w(z)}\right] G_l\left(\frac{\sqrt{2}x}{w(z)}\right) G_m\left(\frac{\sqrt{2}y}{w(z)}\right) \times \exp\left[-ikz - ik\frac{x^2+y^2}{2R(z)} + i(l+m+1)\zeta(z)\right] \quad (2.15)$$

where

$$G_l(u) = H_l(u)e^{(-u^2/2)}$$

is known as the HG-function. $H_l$ and $H_m$ are Hermite polynomials. The first few Hermite polynomials equal

$$H_0(x) = 1, \quad H_1(x) = 2x, \quad H_2(x) = 4x^2 - 2 \quad \text{and} \quad H_3(x) = 8x^3 - 12. \quad (2.16)$$

Figure 2.7 represents intensity distribution of few lower order HG modes. The $HG_{00}$ mode where the Hermite polynomials is equal to 1, is the fundamental $TEM_{00}$ or Gaussian mode. Similar to HG modes, the paraxial wave equation allows other higher-order solutions, with Laguerre-Gaussian modes being among the significant ones. The key takeaway is that in complex optical systems featuring multiple resonating cavities, HOMs may resonate within the system. The primary role of the PC is to identify the presence of HOMs and correct for them.

## 2.4. Stigmatic & Astigmatic Beams

When discussing laser beams in their fundamental mode, it's common to assume they are stigmatic. This means the beam radius is the same in both the x and y directions. Such beams are rotationally symmetric, producing circular spots, and have spherical or planar wavefronts at all points along the propagation axis. However, this is not the general case/configuration for a Gaussian beam [10, 12, 13]. Deviations in the wavefront shapes and beam spot sizes introduce us to simple (or orthogonal) and

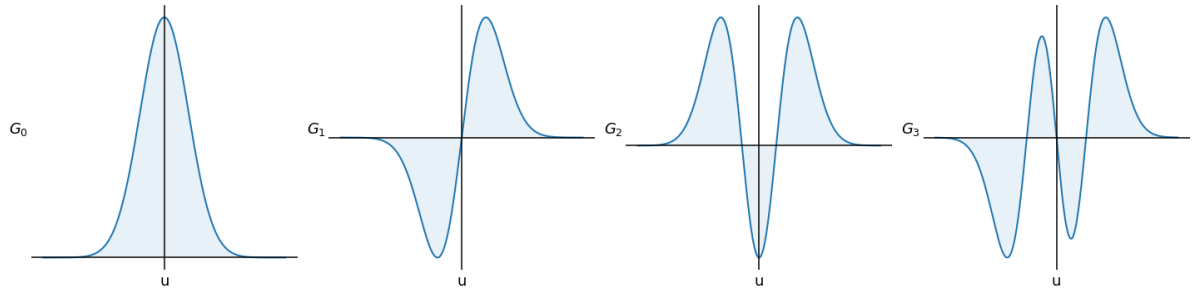


**Figure 2.6:** Lower order Hermite-Gaussian functions.

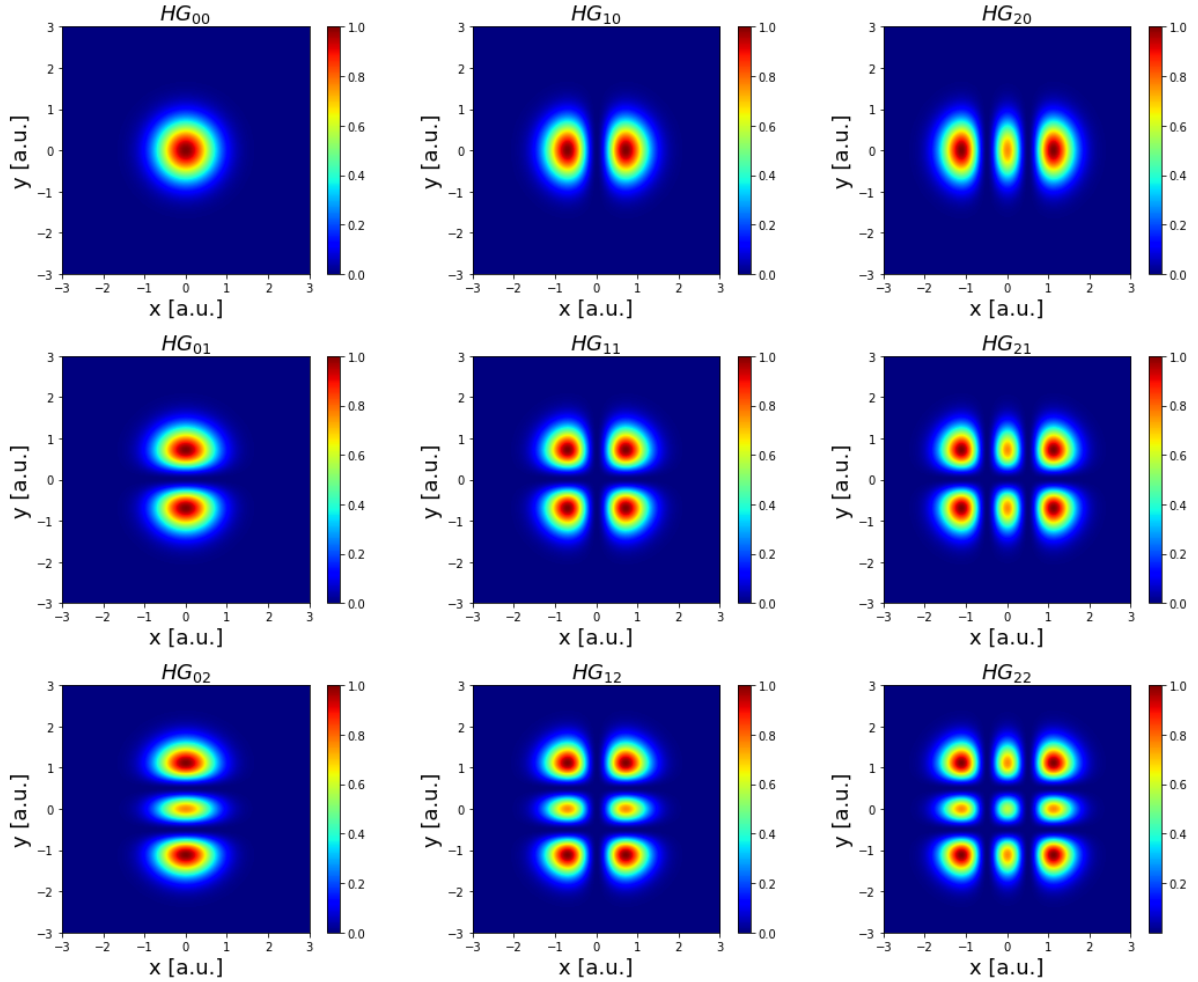


**Figure 2.7:** Intensity distribution of first few Hermite-Gaussian beams. The $HG_{00}$ represents the fundamental Gaussian beam.

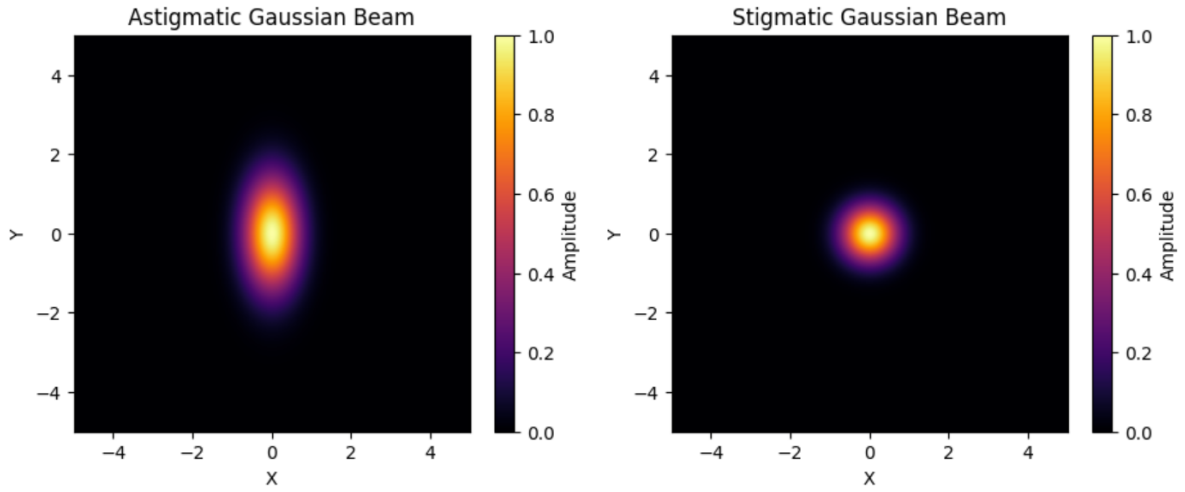


**Figure 2.8:** Fundamental difference between stigmatic and astigmatic beam spots.

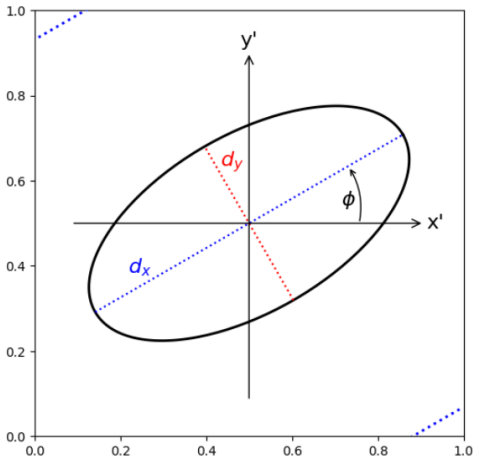


**Figure 2.9:** A schematic representing the nature of astigmatic beams. In the plot, the x'and y'represent the laboratory coordinate system, where as dx and dy represent the beam coordinate system. $\phi$ represents the angle between the two coordinate systems.

general astigmatic beams. To illustrate the difference, figure 2.8 portrays a comparison between the two types of beams, where an astigmatic beam is characterized by an elliptical spot, indicating differing waist radii in the x and y directions. This section will focus on the nuances between the two different kinds of astigmatic Gaussian beams, a topic of relevance given the presence of astigmatism in our laser beam within the prototype PC setup.

A simple or orthogonal astigmatic Gaussian beam possesses two principal widths in the transverse plane that are unequal, resulting in elliptical spots and correspondingly elliptical (or hyperboloidal) wavefronts at every point along its propagation path [10, 12]. Another variable that may emerge in such beams is the tilt of the principal widths relative to the laboratory coordinate system. Figure 2.9 illustrates the characteristics of astigmatic beams, showing how the laboratory coordinate system (x' and y') and the beam's reference system (dx and dy), which is aligned with the beam's symmetry, are tilted with respect to one another. Simple astigmatic beams may be tilted, but this tilt angle ($\phi$) remaining constant along the optical axis [12]. The evolution of an orthogonal astigmatic beam is depicted in figure 2.10. The characteristic behavior of these beams enables the decomposition of the two widths into independent Gaussian evolutions. These widths converge to equal lengths at two points, resulting in a circular irradiance pattern. At each point along the propagation where a circular irradiance pattern is achieved, the ellipticity of the irradiance profile undergoes a shift, swapping the directions (or roles) of the long and the short semi axis.

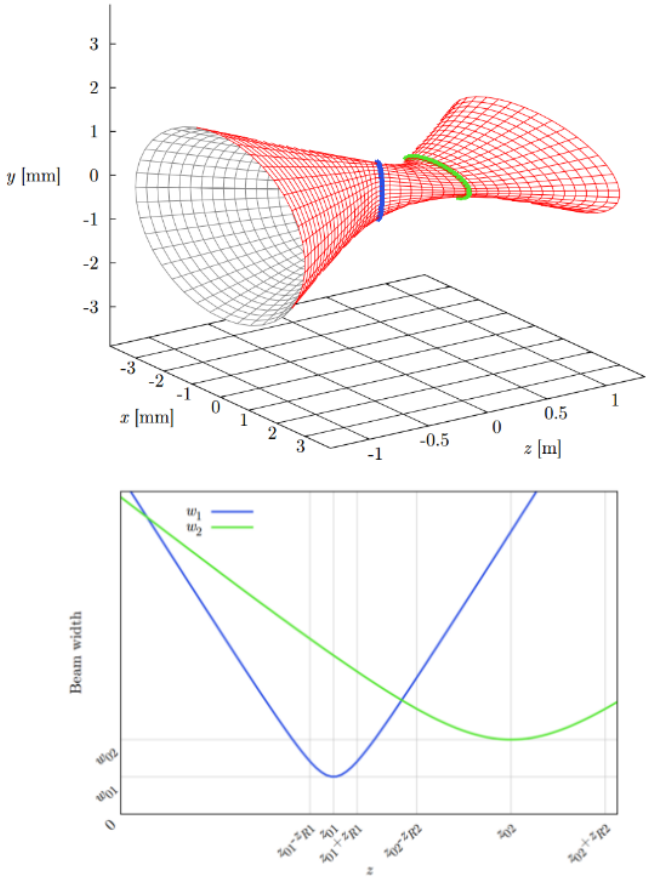


**Figure 2.10:** The 3D representation illustrates the evolution of simple or orthogonal astigmatic beams, accompanied by a plot of the beam size evolution, which is decomposed into two independent Gaussian transformation [12].

In the case of general astigmatic beams, elliptical light spots and ellipsoidal wavefronts are preserved. However the ellipses of constant intensity and those of constant phase do not maintain a fixed orientation throughout propagation. Furthermore, the orientation of the elliptical light spots does not align with that of the ellipsoidal wavefronts at any point along the beam axis [12, 13]. Their relative orientations shift as the beam advances, adding complexity to the beam's behavior. A notable characteristic of these beams is that the elliptical irradiance pattern rotates along the propagation axis.

Astigmatism in a laser beam often stems from imperfections or misalignments in the optical elements through which the beam propagates. For example, when a beam passes through a cylindrical lens, its beam size changes in the plane corresponding to the lens's focal power, while it remains unchanged in the perpendicular plane. Additionally, astigmatism can arise from differing curvatures on orthogonal axes of optical elements, leading to varying focal lengths and causing the beam to converge or diverge unevenly [12]. Factors such as non-uniform refractive indices or thermal effects in optical materials can also contribute to astigmatism. Given the ubiquity of slight misalignments in optical systems, both simple and general astigmatic beams are common occurrences.

# 3

# Phase Camera

The phase camera is a diagnostic tool designed to measure the wavefronts of optical laser beams. It operates based on the principles of heterodyne technique. Its principle purpose is to spatially profile the amplitude and phase of laser beam wavefronts and ascertain their mode content. The initial development of the PC was motivated by the need to separately measure the spatial modes of the carrier and phase-modulated (PM) sidebands exiting the output ports of a GW interferometer [14]. PM sidebands are essential for maintaining (or controlling) the cavities of the interferometer at the desired resonance and for keeping the interferometer at the dark fringe. These control signals are sensitive to cavity misalignments and other optical abberations that alter the spatial modes of the sideband frequencies differently from the main carrier field [14]. Hence probing these PM sidebands independently becomes crucial as they allow better determining the interferometer condition, and helps stabilizing the control of the interferometer [4]. Various wavefront-sensing techniques are commonly employed to examine the spatial profiles and modes of laser beams. The uniqueness of the PC stems from its ability to independently probe and image the spatial profiles for all the radio-frequency (RF) sidebands simultaneously. A comparative overview of different wavefront sensing techniques and their capabilities can be found in table 3.1. For this research we are mainly interested in improving the phase resolution of the prototype PC setup.

Before discussing the working principles of the PC, we will briefly explain the scientific objectives pursued with this tool, particularly its application in AdV. Under ideal conditions, AdV operates with the fundamental transverse electromagnetic mode ($TEM_{00}$) in its cavities. Nonetheless, there is a potential for HOMs to resonate within these cavities. These HOMs may be caused by factors such as misalignments, surface and substrate inhomogeneities, cavity mode mismatches, thermal lensing effects, and other optical abberations. HOMs that arise from sources other than misalignments can disrupt the alignment control and reduce the sensitivity of the detectors [2, 4]. In order to tackle the problem of HOMs resonating in the interferometer due to optical aberrations, a thermal compensation system (TCS) has been developed and commissioned at the AdV. The PC is employed in the TCS as a wavefront sensor to study the HOMs present in the RF beat signal and PM sidebands, and correct for the optical abberations which caused them.

**Table 3.1:** Summary of the capabilities of different wavefront sensors portraying the uniqueness of the PC and its ability to probe all the sideband frequencies simultaneously [2].

| Sensor | Sensitivity of Sidebands | Phase Resolution | Image Points |
|---|---|---|---|
| Shearing Interferometer | cannot distinguish | $\lambda/160$ | |
| Hartmann sensor | cannot distinguish | $\lambda/2000$ | 1024 $\times$ 1024 |
| Time of flight camera | one field at a time | $\lambda/500$ | 200 $\times$ 200 |
| Phase Camera | all fields simultaneously | < $\lambda/500$ | $\geq$ 16,384 |

In this chapter, we will primarily define the working principle of the PC and its prototype optical setup at Nikhef. During this discussion we will highlight the optical arrangement and configuration that is relevant to this work.

## 3.1. Working Principle of the Phase Camera

The working principle of the PC, as shown in figure 3.1, employs a heterodyne technique. The input laser beam is split into two arms by a beam splitter. The reference beam is frequency shifted by 80 MHz ($f_h$) using an acoustic-optic modulator (AOM). This is the characteristic property of heterodyne principle where one of the beams is frequency shifted. The test beam on the other hand is phase modulated by many electro-optic modulators (EOMs) which generates the PM sidebands ($f_s$). As discussed during the start of this chapter, these PM sidebands are used for controlling the interferometer. Both these beams are recombined again at the beam splitter (BS). Optical interference of the test and reference beam yields a beat signal at the heterodyne frequency, 80 MHz, and sum and difference of the heterodyne frequency and the PM sidebands (beat notes). This signal is captured by the photodiode and finally demodulated at the desired radio frequencies.

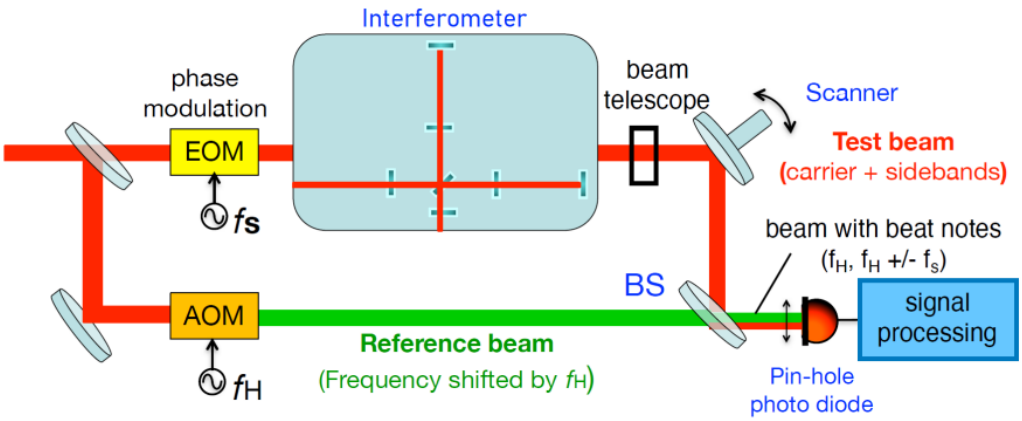


**Figure 3.1:** Working principle of the phase camera [4].

## 3.2. Optical Setup of the Phase Camera

The optical layout of the prototype PC setup at Nikhef is shown in figure 3.2 and 3.3. For this research, we use a Nd:YAG laser (Mephisto 500 mW YAG Laser System by Coherent) with a wavelength of 1064 nm and a total power of 500 mW. Although the layout depicts the laser beam entering the interferometer directly, in reality, the beam is preconditioned and passes through multiple optics, covering significant optical path lengths before actually entering the PC setup. Additionally, the laser beam is shared with multiple optical setups on the bench, resulting in a beam power of about 160 mW in the PC setup. The beam enters the setup through an iris, which serves to remove any potential beam halo due to reflections. It is then split into two arms of the interferometer by beam splitter BS1. For our setup, the split ratio is not exactly 50:50; instead, the reference beam and the test beam has a total power of 82 mW and the 48 mW respectively. The diverging reference beam is collimated by lens L1 with a focal length of 500 mm. With mirrors M1 and M2, the beam is steered to the input collimator (Thorlabs TC18APC-1064) and a single-mode polarization-maintaining optical fiber cable (Thorlabs P3-1064PM-FC-1). The beam travels through this fiber to an AOM (AA Opto-Electronic MT80-IR60-Fio-PM0,5-J3V-A), which shifts the frequency of the input beam by 80 MHz (heterodyne frequency). After exiting the output collimator, the beam emerges nearly non-divergent (collimated) and is directed towards beam splitter BS3 and the photodiode. At BS3, this beam interferes with the test beam, which travels along the other arm of the interferometer.

The test beam is the one which passes through (and not reflected) by BS1. The lens L2 of focal length 200 mm is strategically placed to focus the beam size to match the pinhole diameter of the EOM (Qubig PS2M-NIR). The test beam is steered towards the EOM which phase modulates the input beam at the

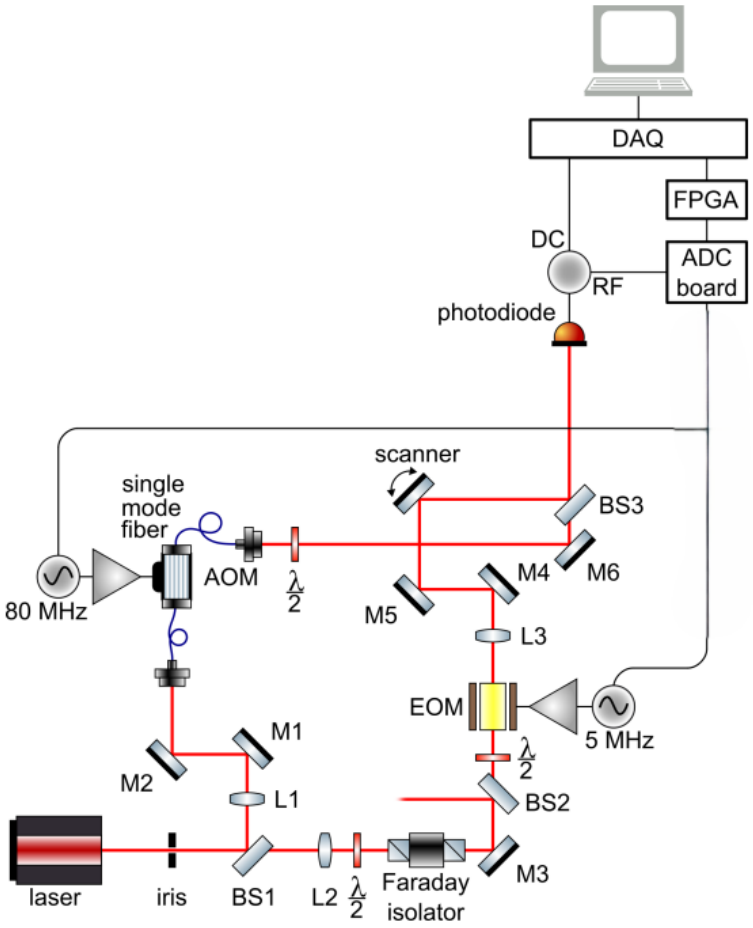


**Figure 3.2:** Schematic of the prototype optical setup of the PC [6].

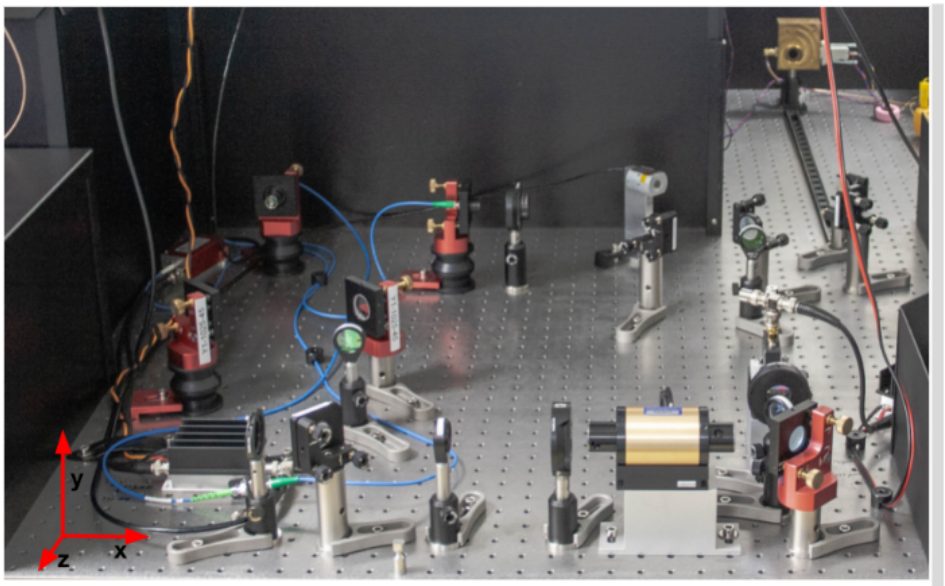


**Figure 3.3:** The actual prototype PC setup at Nikhef [6].

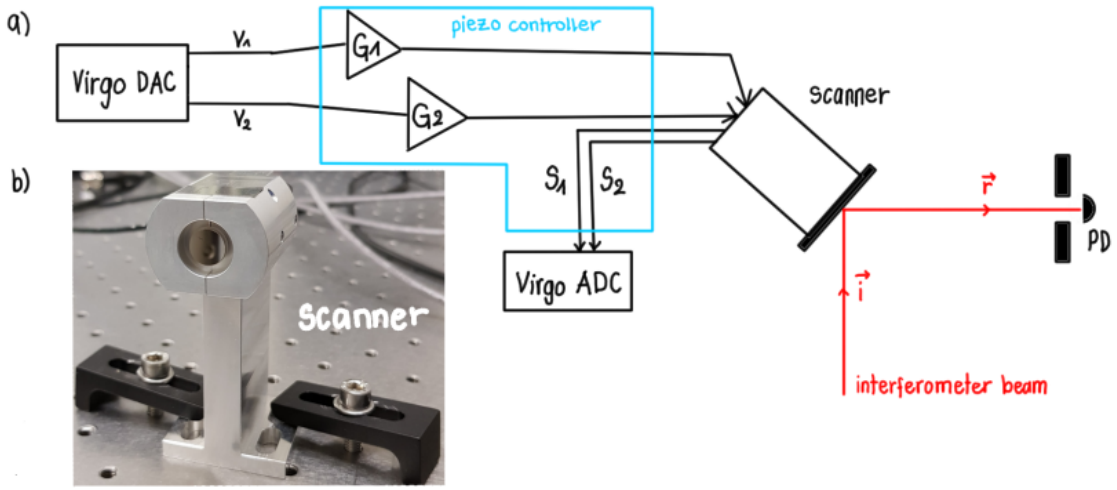


**Figure 3.4:** (a) Schematic of the scanner along with its working principle, (b) Image of the real scanner used in the PC setup [2].

desired frequency and generates the so called sidebands, if viewed in the frequency spectrum of the modulated beam. These sidebands have a special purpose and role to play in AdV, and we are just trying to mimic the same setup. Before the EOM, a Faraday isolator is placed to protect other optical setups on the bench from unwanted back-reflection of the beam. The output beam of the EOM is then collimated by lens L3 of focal length 300 mm. By using mirror M4 and M5, the beam is steered towards the scanner (Physik Instrumente S-334-2SL). The scanner is important for obtaining 2D phase and amplitude maps (images) of the wavefronts of the test beam, particularly by scanning (or moving) the beam over the pinhole photodiode. Figure 3.4 provides a rough schematic and an image of the scanner used in the PC setup. The scanner consists of a servo system to measure the position of the mirror and using actuation voltages applied to piezo-elements, it can tip-tilt the mirror. Finally, the scanner reflects the test beam to the BS3, where it recombines with the reference beam. The recombined and interfered beam is then detected by the photodiode (OSI Optoelectronics FCI-InGaAs-55), which has an active area diameter of 55 $\mu$m. Finally, the signal measured by the photodiode is digitized by a 14-bit analog-to-digital converter (ADC) and is demodulated digitally by an field programmable gate array (FPGA) box and further data processing is done in a system similar to the AdV real-time system.

Now that we have established the working principle of the prototype PC setup, we will explain the scientific formulation and data acquisition of the signal measured by the photodiode.

### 3.2.1. Formulation

The photodiode in the PC setup truly measures the intensity of the interference of the test beam $E_c$ and the reference beam $E_{ref}$, as shown in figure 3.5. The two beams in the setup are Gaussian ($TEM_{00}$) and the electric field intensity can be described by the equation 2.8. The test beam consists of the carrier with optical frequency $f_c$ and also includes sideband or phase-modulated frequencies. $f_c$ represents the frequency of the input laser beam (1064 nm). The reference beam is frequency shifted with respect to the input beam by the heterodyne frequency $f_h$, such that the resulting frequency of the beam is given by $f_{ref} = f_c + f_h$. Assuming no sideband frequencies for simplicity, the intensity measured at the photodiode can be expressed as follows:

$$\begin{aligned} I(x,y) &= |E_c(x,y) + E_{ref}(x,y)|^2 \\ &= |E_c(x,y)|^2 + |E_{ref}(x,y)|^2 \\ &\quad + 2|E_c(x,y)||E_{ref}(x,y)| \cos(2\pi f_h t + (\phi_{ref} - \phi_c)) \end{aligned} \tag{3.1}$$

The intensity distribution I(x,y), can be represented by two components: a DC term, which is the sum of the squares of the individual electric field distributions, and the PC-term or RF-term, which is the result of the cross product of $E_c$ and $E_{ref}$, and is given by:

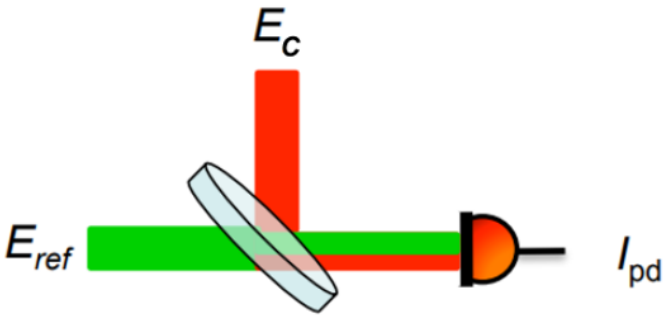


**Figure 3.5:** The optical intensity measured by the photodiode.

$$2|E_c(x,y)||E_{ref}(x,y)|\cos(2\pi f_h t + (\phi_{ref} - \phi_c))$$

In the RF-term $(\phi_{ref} - \phi_c)$ represents the phase difference between the reference and test beams. Given that these beams are Gaussian, the phase difference term incorporates the Guoy phase, RoC, and linear phase variation as explained in section 2.2.1. $\phi_{ref}$ and $\phi_c$, specifically represent the phase accumulated by the beams in their respective arms. In the photodiode amplifier this DC and RF component of the input signal are split and amplified as shown in figure 3.2. The RF signals are digitized by an ADC board and then digitally demodulated at the heterodyne frequency of 80 MHz. The DC signals are acquired by Virgo-style ADCs and are primarily used for alignment purposes.

### 3.2.2. Data Acquisition and Digital Demodulation

The beat signal, or RF signal, along with the reference signals that drive the EOM and AOM, are sampled by a 500 MS/s 14-bit ADC board and then digitally demodulated by a FPGA. Our primary interest lies in the demodulation of the beat signal at 80 MHz. The PC is designed primarily to image the wavefronts of optical beams. Each image consists of 16,384 pixels. Each pixel in the image is constructed using 16,384 ($2^{14}$) ADC samples, meaning that 16,384 ADC samples are used to compute a phase value per demodulation frequency for each pixel. In our prototype setup, the total measurement/scanning time is $2 \times 10^{-9}$ s $\times$ 16384 samples $\times$ 16384 pixels $\simeq$ 0.537 s. Here, 2 ns represents the sampling frequency (or interval), and 16,384 is both the number of ADC samples per pixel and the total number of pixels used to image the beam. The entire measurement time for scanning is less than 1 second because all data in the Virgo DAQ system is stored in frames with a duration of 1 second. In summary, the phase of the optical wavefronts is measured 16,384 times within a total measurement time of 0.537 seconds.

After the input RF-signal is digitized by the ADC, the accumulated ADC samples for each pixel are processed through a Hann window function. Subsequently, these samples are multiplied by a sine and cosine of the demodulation frequency. This data is then summed, which acts as a form of time integration and as a low-pass filter. This process results in the in-phase (I) and quadrature (Q) components of the measured signal, a technique commonly referred to as I-Q demodulation. Finally, the amplitude for each pixel or measurement is calculated by taking the square root of the sum of the squared I and Q components and the phase for each pixel is determined by taking the arc-tangent of the ratio of Q to I.

$$A = \sqrt{I^2 + Q^2} \tag{3.2}$$

$$\phi = \arctan\left(\frac{Q}{I}\right) \tag{3.3}$$

The obtained phase value ($\phi$) represents the phase difference between the test and reference beams of our interferometer setup, as shown in equation 3.1. In parallel to the RF-signal, the electrical reference

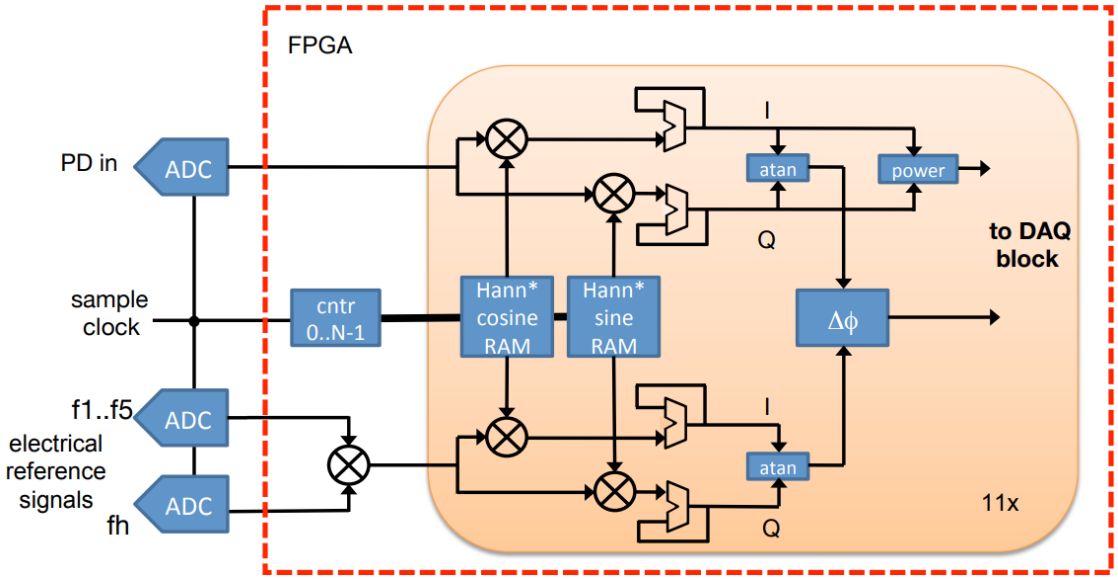


**Figure 3.6:** Digital demodulation technique adopted for the PC setup.

signal from the AOM and EOM is also demodulated with the same process. This reference signal provides the phase reference for the demodulated RF-signal. Since we are performing differential phase measurements, the reference phase is subtracted from the measured phase to get the relative phase of the measured wavefront [2]. This complete digital demodulation process is represented in figure 3.6. In the figure $\Delta\phi$ represents the difference between the demodulated phase of the RF signal and the reference signals.

This chapter describes the general setup of the PC and its working principle, based on its research and science goals. The explanation also outlines the technique for conducting phase measurements using the PC and extracting phase values through the digital demodulation technique. Each set of phase measurements consists of 16,384 subsequent readings, taken over a duration of 0.53 seconds. The scope of this research is exclusively on understanding the relative phase measurements of the heterodyne beat signal, without probing the sideband frequencies. The overall goal of this work is to understand the fluctuations in $\Delta\phi$ over a short time span within the entire measurement period. We are also not interested in imaging the wavefronts; therefore, the scanner is not actuated to scan the beam over the photodiode. Throughout all phase measurements presented in this work, EOM does not modulate the test beam, and the scanner is not actuated. Instead, all phase measurements are conducted with the scanner mirror in a fixed position, effectively functioning as a plain mirror. This method of measurement is referred to as static phase measurement.

# 4

# Phase Camera Setup Characterization

In chapter 3, we introduced the prototype phase camera setup. A pertinent question now emerges: how accurately is the setup functioning? The accuracy of the setup and its performance can be affected by factors like laser beam drifts, mechanical drifts, and other environmental factors. These factors directly impact the laser beam's quality, resulting in issues such as clipping, pronounced astigmatism in beam spots, and improper overlap of the two beams at the beam splitter. The beam quality plays an important role in the overall interference signal produced and phase measurements. Thus, our aim is to characterize the interferometer setup to assess its operational accuracy and ensure it meets its design criteria. Characterization, in this context, involves measuring and quantifying the laser beam's properties and nature within the setup.

In this chapter, our focus will be on the results from beam profiling of the laser beams in both the arms of the interferometer. We will also assess the accuracy by comparing our results to calculations (ABCD matrix 2.2.2) based on ideal conditions.

## 4.1. Beam Profiling

In this research, we used a CCD camera (CinCam CMOS-1.001-Nano) to capture the intensity profile (or distribution) of the laser beam at various positions along the propagation axis. It is a high resolution camera featuring a pixel size of 5.5 $\mu m$ with a total pixel count of 2040 $\times$ 2040. The total size of the camera's focal/detector plane is $11.22 \times 11.22$ mm$^2$. For all the measurements the camera's configurations/settings was kept the same. To prevent saturation of the pixels, we employed neutral density (ND) filters with varying optical densities to attenuate the beam's power. The analysis & modelling of the beam profile was conducted using the raw pixel data collected from the camera.

To have background calibrated measurements, we recorded the camera's baseline levels by capturing 64 dark frames. A dark frame, acquired with the camera's shutter closed, quantifies the camera's inherent noise, commonly known as thermal noise or dark current. This dark current contributes to a baseline noise level in all images, potentially diminishing measurement precision. By averaging these 64 dark frames, we mitigate fluctuations and quite accurately approximate the offset values of each pixel, resulting in a noise-reduced background frame of the CCD. Figure 4.1 plots a histogram of the probability densities of the pixel values of the averaged background frames, alongside the difference between an individual background measurement and the averaged frame. The noise level of the CCD camera, represented by the standard deviation of the Gaussian fit as shown in figure 4.1b, is 1.18 (standard error = 0.00040) in pixel value (arbitrary units). Subsequently, the averaged frame was subtracted from every measurement, on a pixel-by-pixel basis. This improves the precision of the beam measurements.

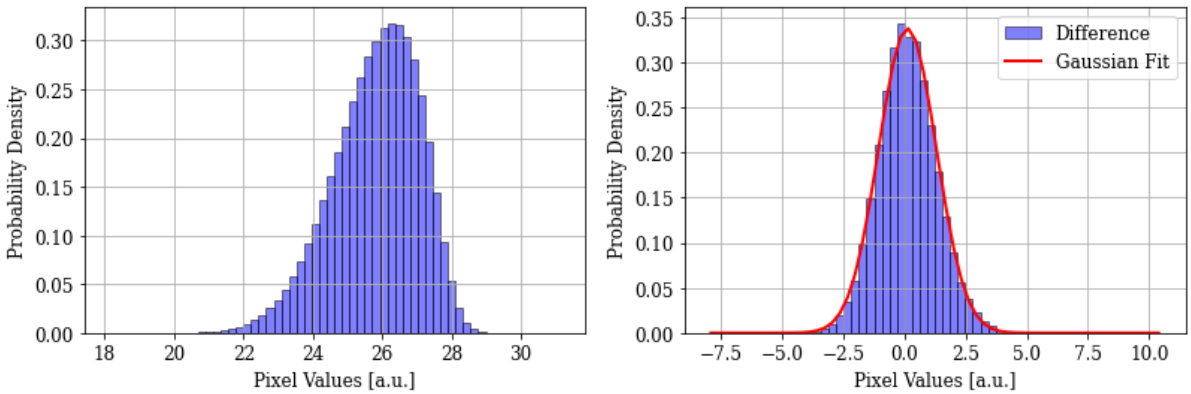


**Figure 4.1:** Results from the CCD camera's background measurements: a) Histogram of the pixel to pixel offset; b) Histogram of the difference between the averaged frame and a single background measurement, along with a Gaussian fit. The standard deviation of the distribution is 1.18 pixel value [a.u.].

### 4.1.1. Reference Beam Characterization

To characterize the reference beam, we divided its path into two segments. Figure 3.2 illustrates the optical setup of the PC. The reference plane for our measurements is established at the lens, prior to the PC setup. Note that the lens (reference plane) itself is not depicted in the figure. The first part extends from the reference plane to the input collimator, and the second part spans from the output collimator to the photodiode. We analyze this beam path in segments due to the presence of an optical fiber cable within it. The beam's propagation through the fiber is not modeled, with the output beam accepted as a given. For clarity, we will examine these segments individually.

#### Part 1

For the first part of the reference beam 28 measurements were taken along the optical path, starting from the reference plane (lens of f=250 mm) up to the input collimator. The measurements for this part takes into account of the beam entering PC setup or input beam. Our objective was to characterize the beam's properties at each measurement point, and evaluate its propagation behaviour. To achieve this, we require information about the beam's waist size and position (w.r.t. to the reference plane). The following information is sufficient to have a complete knowledge of the beam.

Figure 4.2 shows beam spots (intensity distribution) from various measurements at different positions w.r.t. the reference plane, scaled according to the camera's dimensions. An initial analysis of the figures indicates a trend where the beam spot size first decreases and then increases along the propagation axis, hinting the location of the beam waist within this region. The consistency in beam spots across measurements suggests a stable laser output. Notably, the spots exhibit good circular symmetry (stigmatic), indicative of a $TEM_{00}$ (Gaussian) mode. The presence of visible interference patterns/fringes and Newton rings, especially in larger spots, could be attributed to light interference from scratches and dust on the CCD detector or ND filters. Given that we employ several of these filters to attenuate power, it is highly probable that the observed patterns result from the filters themselves, representing artifacts of the measurements.

To determine the beam properties, we fitted the beam intensity distribution with a 2D Gaussian function and applied a least-squares curve fitting technique. Fitting 2D Gaussian functions is a common problem across fields such as astronomy, and various methods can be used to address it. We use the over-determined weighted regression method [15, 16] for this purpose. The model function used for fitting purposes describes a general two-dimensional Gaussian function mathematically defined as [16, 17, 18]:

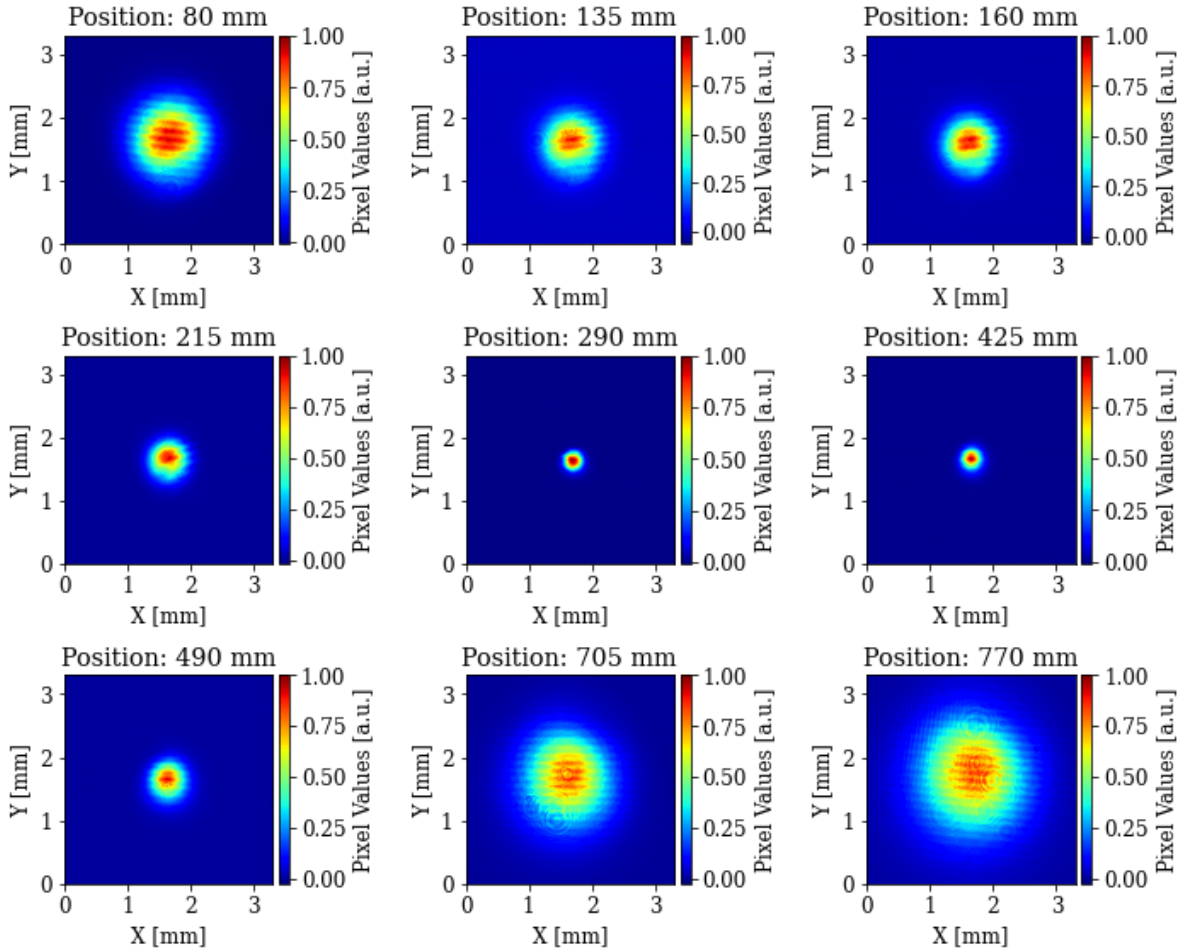


**Figure 4.2:** Transverse profiles of the laser beam from selected positions (w.r.t. reference plane) in part 1 of the setup, displaying cropped versions where the X and Y axes indicate the actual spot sizes in millimeters.

$$
\begin{aligned}
f(x,y) = A \exp \Bigg[ & -(x-x_o)^2 \left( \frac{\cos^2\phi}{2\sigma_x^2} + \frac{\sin^2\phi}{2\sigma_y^2} \right) \\
& -(y-y_o)^2 \left( \frac{\sin^2\phi}{2\sigma_x^2} + \frac{\cos^2\phi}{2\sigma_y^2} \right) \\
& -2(x-x_o)(y-y_o) \left( \frac{\sin 2\phi}{4\sigma_x^2} - \frac{\sin 2\phi}{4\sigma_y^2} \right) \Bigg]
\end{aligned} \tag{4.1}
$$

Herein, the model function incorporates six dependent parameters essential for characterization and two independent parameters, x and y. Parameter A denotes the intensity (or pixel value) of the distribution, while $\sigma_x$ and $\sigma_y$ represent the deviation of the Gaussian distribution in x and y, respectively. The parameter $\phi$ signifies the angle between the lab and beam coordinate systems, as illustrated in figure 2.9, whereas $x_o$ and $y_o$ denote the shift and center of the beam spot, respectively. The size of the beam is defined as twice the deviation of the Gaussian distribution, $2\sigma_x = w_x$ and $2\sigma_y = w_y$. This is because we fit the intensity distribution which is the square of the electric field amplitude, while the beam size ($w_x$ and $w_y$) is defined for the electric field.

Using the Gaussian beam model, as described in equation 4.1, we fit the 2D pixel data. An illustration of such fitting for position 1 (80 mm) is provided in figure 4.3, with the major and minor axes denoting the orientation of the beam axes. This representation highlights the tilt (61.04°) and astigmatism present

in our laser beam. The tilt in the beam axes can be caused by the orientation of the optical elements, which can impose a specific directional bias on the beam. Table 4.1 and table 4.2 display the fit statistics and the standard errors of the fit parameters, respectively. R-squared value close to 1 indicates a strong match between the model and the observed data. The low reduced chi-square value is primarily attributed to the high degree of freedom (D.O.F) in the fit. Additionally, the minimal standard errors associated with the fit parameters reflect precise parameter estimation. However, the standard error in $\phi$ is approximately 0.19°, which is higher than that of other fit parameters. The Gaussian distribution along with the fit across the two independent beam axes is depicted in figure 4.4. We can clearly see there are dips in the distribution, which correspond to the interference fringes. Overall, these statistics shown in table 4.1 and 4.2, affirm the model's effectiveness in accurately representing the laser beam spots. Subsequently, the residual analysis of the fit for measurement position 1 & 5 (290 mm), is depicted in figure 4.5.

**Table 4.1:** Statistical analysis of the 2D Gaussian fit for measurement position 1.

| Statistical Measure | Value |
|---|---|
| Chi-square ($\chi^2$) | 97.220 |
| D.O.F | 360000 |
| Reduced chi-square ($\chi^2_{\text{red}}$) | $2.70 \times 10^{-4}$ |
| Coefficient of Determination ($R^2$) | 0.9906 |

**Table 4.2:** Parameter estimates from the 2D Gaussian fit and their standard errors, for measurement position 1.

| Parameters | Estimated Value | Standard Error |
|---|---|---|
| A | 0.89 a.u. | $0.2 \times 10^{-3}$ a.u. |
| $x_0$ | 1.65 mm | $0.8 \times 10^{-4}$ mm |
| $y_0$ | 1.66 mm | $0.8 \times 10^{-4}$ mm |
| $\sigma_x$ | 0.38 mm | $0.82 \times 10^{-4}$ mm |
| $\sigma_y$ | 0.39 mm | $0.8 \times 10^{-4}$ mm |
| $\phi$ | 61.04° | 0.19° |

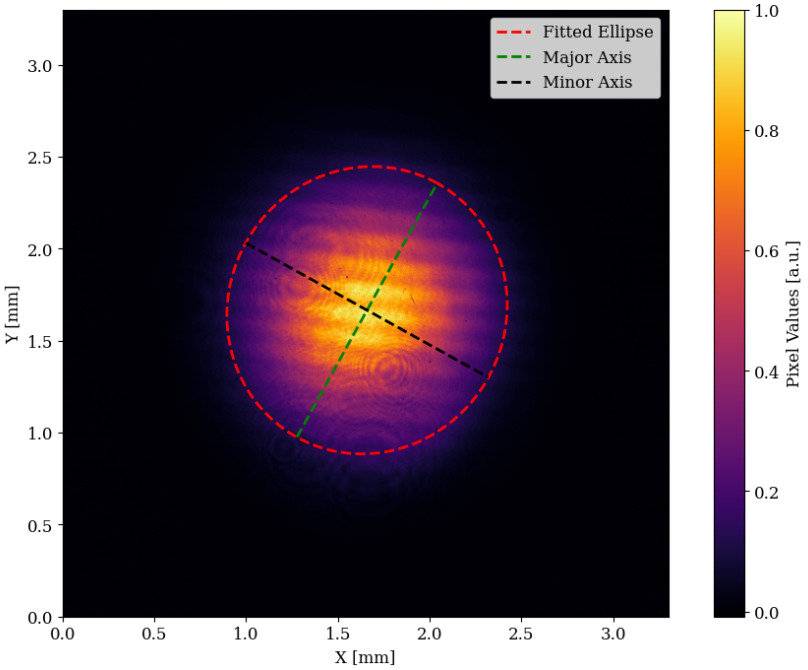


**Figure 4.3:** Representation of a 2D Gaussian fit for measurement position 1 of the reference beam, where the major and minor axes represent the beam's symmetry.

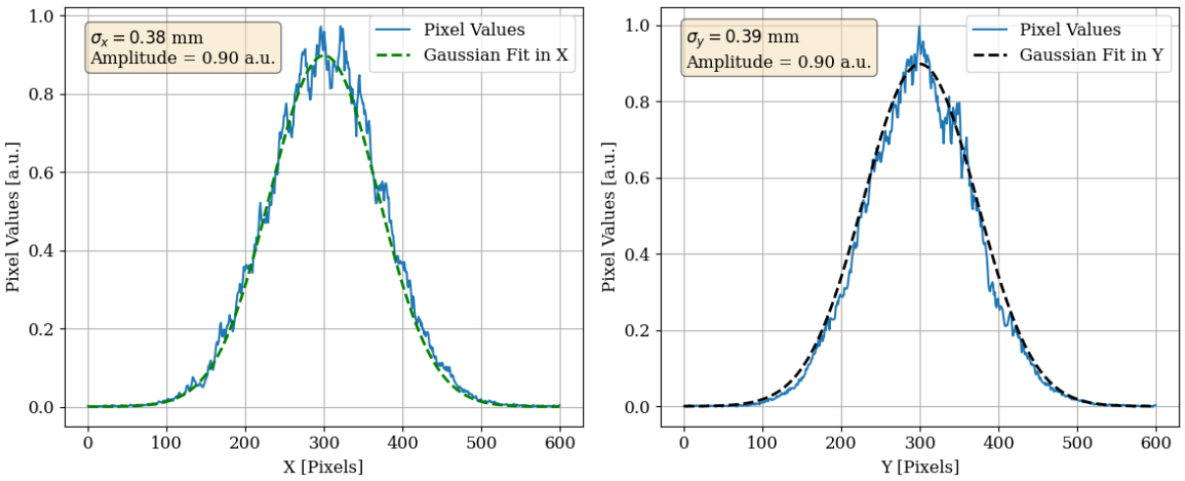


**Figure 4.4:** 2D Gaussian fit along the minor and major axis of the beam at measurement position 1, as shown in figure 4.3. The fit parameters is also represented in the plot.

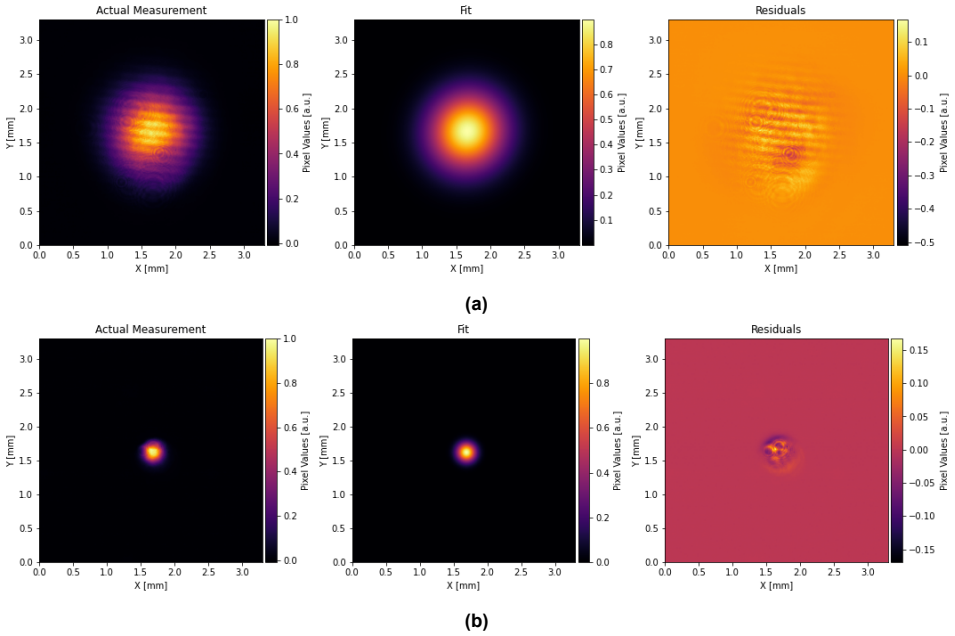


**Figure 4.5:** Residual analysis of the 2D Gaussian fit for (a) Measurement position 1 and (b) Measurement position 5, as shown in figure 4.2.

Our main focus from the measurements was to deduce the beam width (or radius) parameters, $w_x$ and $w_y$. For our purpose, we assume the beam in our setup to be simple astigmatic and hence the width estimates in the x and y directions will be decoupled from each other and will be evaluated independently. The width estimates from all the measurements of part 1 are plotted in figure 4.6. A noticeable discontinuity in the width beyond 800 mm aligns with the presence of collimating lens (f = 500 mm) in the setup. Additionally, attention should be given to the interchange of the $w_x$ and $w_y$ as major and minor widths once the beam begins to diverge after reaching its waist (minimum). This behavior is a defining characteristic of astigmatic beams, as detailed in section 2.4.

To determine the beam waist and position of it with respect to the reference plane, we use the equation 2.9, to fit a curve to the measurement points as shown in figure 4.6. Here we are interested only in the input beam (diverging beam). The fit along with the measurement points is represented in figure 4.7. Parameters $z_{xo}$ and $z_{yo}$ represent the waist location, and are indicated by the vertical lines. The

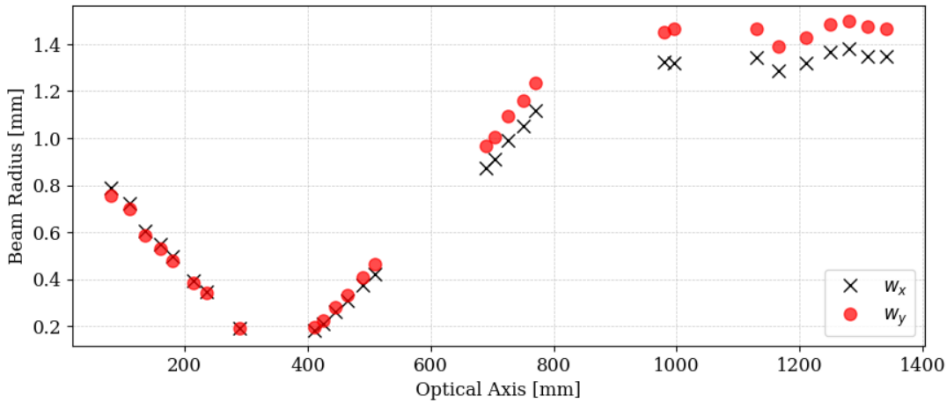


**Figure 4.6:** Beam width measurements for the two independent Gaussian evolutions in x and y directions.

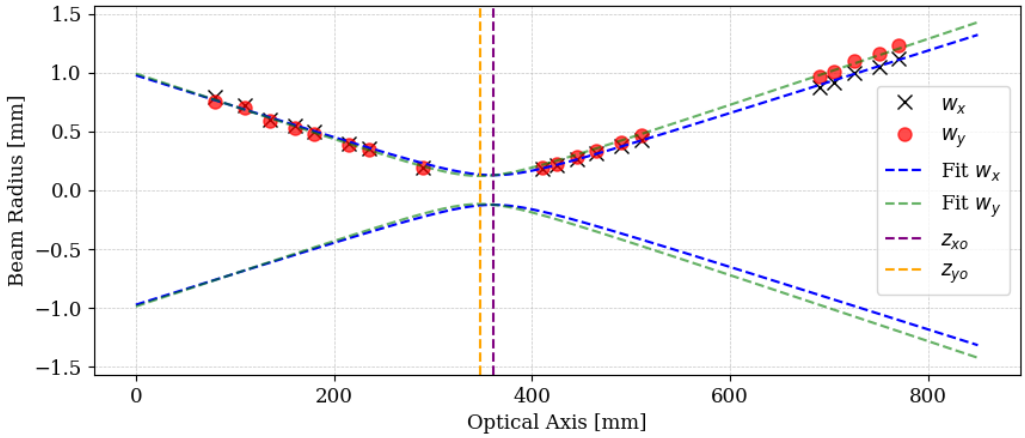


**Figure 4.7:** Fit of the width measurements shown in figure 4.6. The fit estimates is represented in table 4.3.

characteristics obtained from the fit are summarized in table 4.3. One thing to note is that the equation 2.9 inherently assumes the $M^2$ of the beam to be 1. There are other ways to fit the beam radius points in which we can model the $M^2$ to be one of the fit parameters. The problem is that the $M^2$ is correlated with other beam parameters. Anyhow, the $M^2$ of our laser beam is less than 1.1 [19]. Since these represent very rough measurements not following the ISO standards, for simplicity we assume the $M^2$ = 1. The difference between the two waist position is minimal, 13.19 mm, hence the beams are highly stigmatic.

**Table 4.3:** Waist size and location (w.r.t. reference plane) of the input beam entering the interferometer.

| Beam Properties | | |
|---|---|---|
| Waist size [mm] | $w_x = 0.1260 \pm 0.0008$ | $w_y = 0.1196 \pm 0.0008$ |
| Waist location [mm] | $z_{xo} = 360.57 \pm 1.6$ | $z_{yo} = 347.38 \pm 1.5$ |

In the reference beam arm, post-splitting, the beam passes through a lens with a focal length of 500 mm, aimed at collimating the beam before it enters the input collimator of the AOM. Figure 4.8 showcases the beam's collimation; the slopes of the fitted lines gives a divergence angle of $0.006°$ for x and $0.004°$ for y, reflecting a high degree of collimation. The spots exhibit uniform size with slight variations. Given the consistent shape/collimation of the beam in this segment, the calculated mean and standard deviations for $w_x$ and $w_y$ are $1.33 \pm 0.026$ mm and $1.45 \pm 0.031$ mm, respectively. The values are a good approximation of the radius of the beam entering the input collimator.

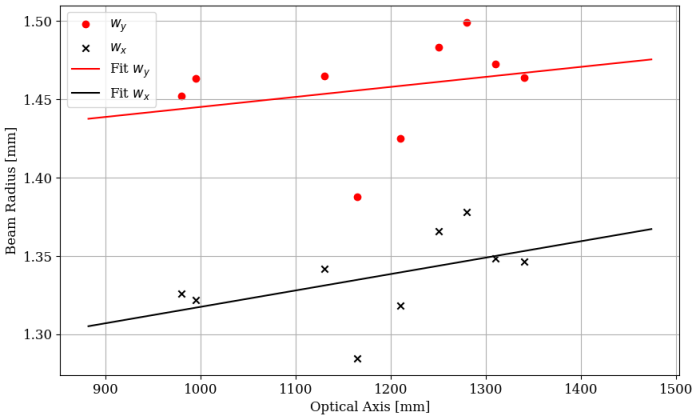


**Figure 4.8:** Degree of collimation of the beam before entering the input collimator with slope of the fitted line being $0.006°$ for x and $0.004°$ for y.

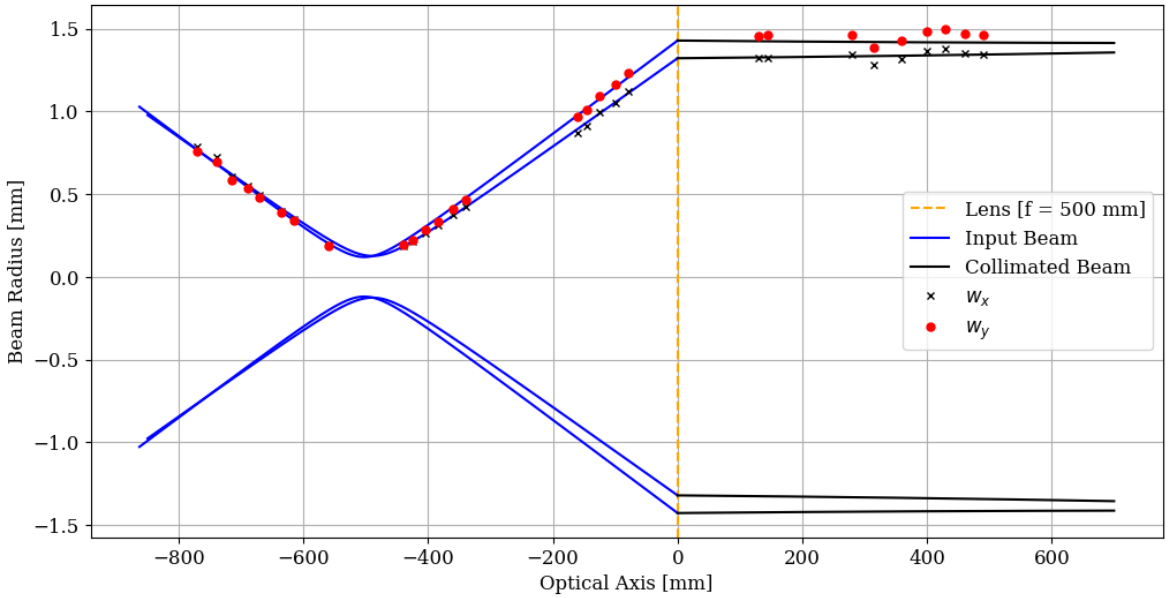


**Figure 4.9:** Calculated ideal beam propagation of the input beam through a 500 mm focal length lens, compared with actual beam measurements obtained using the beam profiler. In the figure the reference plane has been changed to that of the lens (f= 500 mm).

Now, with knowledge of the input beam properties and focal length of the lens, we use the ABCD law to calculate Gaussian beam propagation. Figure 4.9 displays this comparison, showing both the calculated ideal beam propagation and the widths from our beam profiling measurements. The vertical line in the figure marks the plane of the lens, illustrating a clear change in the beam properties at the lens interface. Overall the nature of the beam in the setup matches closely with the calculation.

In conclusion, the beam profiling results from part 1 demonstrate a well-defined Gaussian beam ($TEM_{00}$) and ideal properties. Aside from modeling the beam within the fiber cable, this analysis thoroughly characterizes the beam's behavior and propagation.

Part 2

Part 2 of the reference beam is the beam emerging from the output collimator. We conducted 10 measurements between the output collimator and the photodiode, with the measurements and their corresponding waist estimates shown in figures 4.10 and 4.11, respectively. The beam is well collimated as it exits the output collimator, reaching a beam radius of approximately 1.15-1.20 mm by the time it arrives at the photodiode. The beam displays good stigmatism, and in comparison to the beam

spots observed in part 1, it lacks interference fringes/patterns which were observed earlier. This can be due to the reflective filters used to attenuate the beam power for part 1.

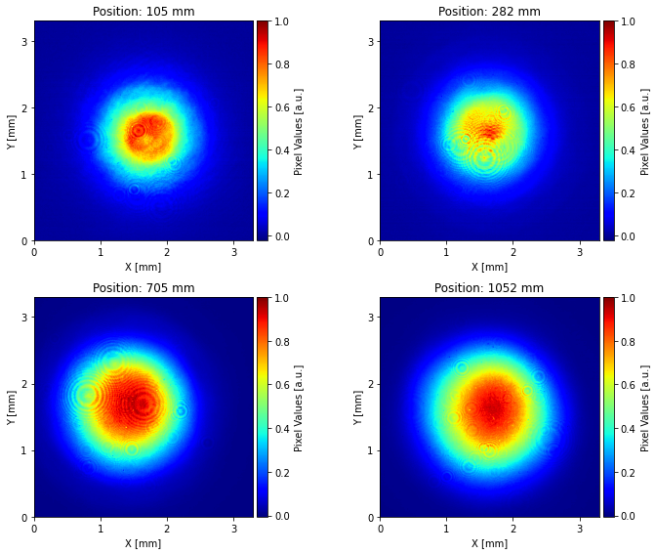


**Figure 4.10:** Results from laser beam profiling of part 2 of the reference beam measurements. The reference plane for the defined positions is the output collimator.

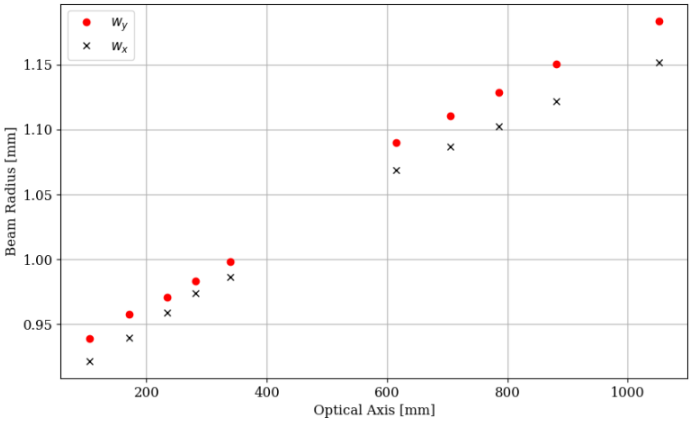


**Figure 4.11:** Beam radius parameters obtained from fitting the measurements of part 2 of the reference beam setup.

This analysis concludes the characterization of the reference beam. The ellipticity values, defined as the ratio of the minor axis to the major axis and indicative of the beam's astigmatism level, are notably close to 1 for the reference beam, as shown in the figure 4.12.

### 4.1.2. Test beam Characterization

To characterize the test beam, we employed a procedure similar to that used for the reference beam; taking 25 measurements along the optical path to understand the beam's behavior. Having extensively covered the analysis for the reference beam, we will briefly present the results for the test beam, focusing primarily on the setup's performance relative to calculations.

Initial observations of the test beam revealed significant astigmatism in its shape, attributed to clipping within the Faraday isolator and the EOM. Upon correcting for the alignment in the setup, we achieved improved beam spot quality, as illustrated in figure 4.13. The measurements shown in the figure cover the path from the scanner to the photodiode, revealing mostly circular beam spots.

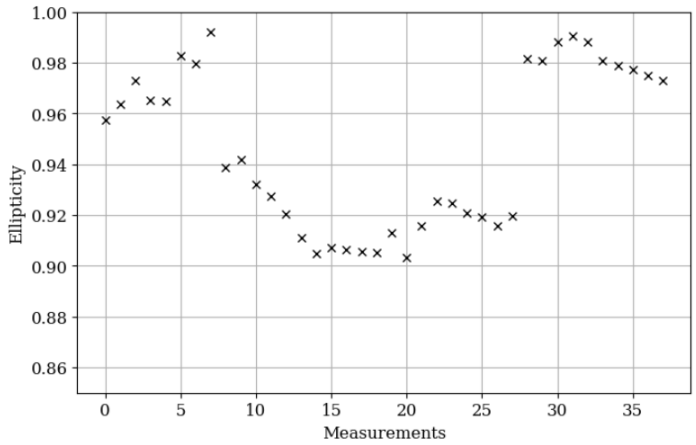


**Figure 4.12:** Ellipticity values obtained for all the measurements of the reference beam. The values indicate a highly stigmatic Gaussian beam.

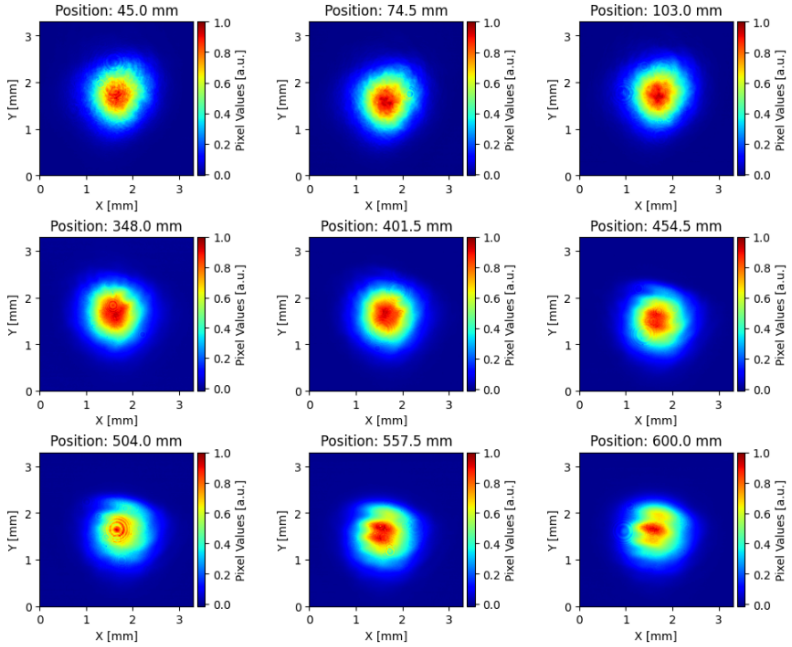


**Figure 4.13:** Beam spots for various measurements of the test beam, after the scanner. The reference plane for the defined position is the scanner.

To validate our beam measurements against theoretical predictions, we applied the ABCD propagation law to the input beam characteristics determined from the reference beam analysis. The estimates of the beam radius obtained from 2D Gaussian fit are shown alongside the calculated Gaussian beam propagation in figure 4.14. Vertical lines within the figure indicate the location of the optical components. The test beam setup includes two lenses with distinct focal lengths: one focuses the beam to match the aperture size of the Faraday isolator and the EOM, while the other aims to collimate the beam before its recombination with the reference beam at the beam splitter. To ensure alignment, the EOM is strategically placed at the waist of the focused beam. Considering the EOM's aperture size of $2 \times 2$ mm$^2$, the waist size of the beam before it enters the EOM is approximately 0.12 mm. Overall, the test beam setup function accurately, as confirmed by the beam measurements.

Compared to the reference beam, the test beam exhibits relatively higher astigmatism. Throughout the experimental work and research, multiple misalignments and beam clippings were observed in the test beam path, particularly noticeable in the output beam from the EOM, despite the beam size

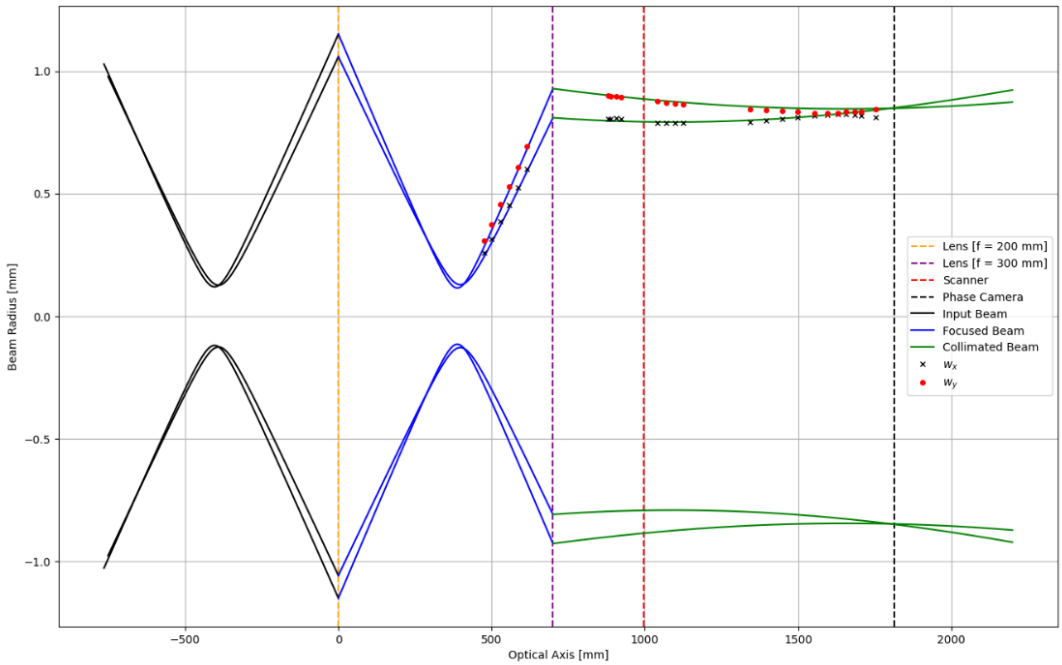


**Figure 4.14:** A complete calculation of the test beam setup is depicted alongside the actual beam measurements, demonstrating that the overall setup aligns accurately with the system's design and functionality.

being significantly smaller than the EOM's aperture. The beam produced by the EOM demonstrates astigmatism, with ellipticity values falling below 0.87, as illustrated in figure 4.15. For the objectives of this thesis, astigmatism does not significantly impact phase measurements; however, for optimal beam quality, a stigmatic beam is preferred. Additionally, to align the setup more closely with the simulations of the PC, spherical wavefronts are desired over the elliptical wavefronts produced by astigmatic beams.

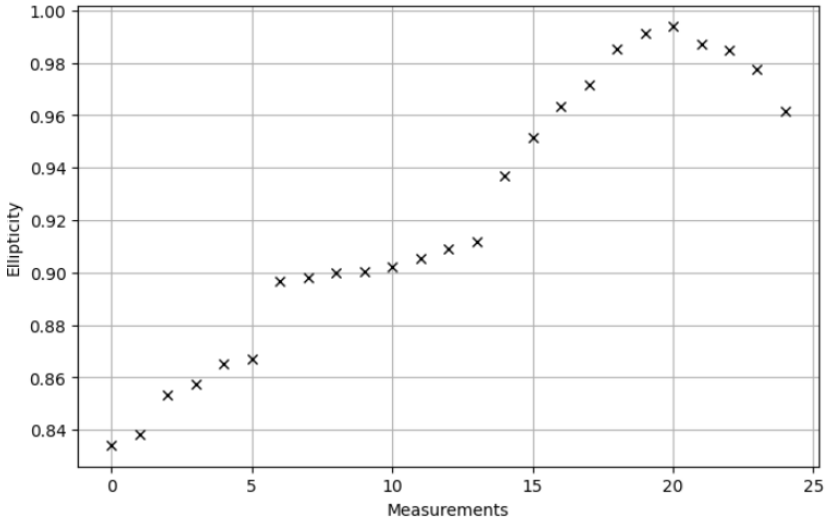


**Figure 4.15:** Ellipticity values for all the measurements of the test beam.

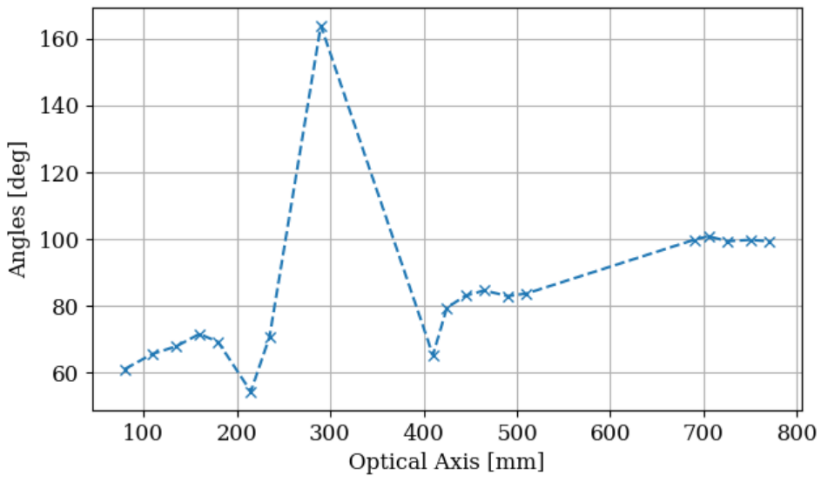


**Figure 4.16:** Angle between the major beam axis and axis of the beam profiler.

### 4.1.3. Discussion

There are additional observations and minor caveats that merit attention. In our analysis, the primary focus was on the beam radius parameters of our Gaussian beam, with minimal discussion on the angles ($\phi$) subtended relative to the laboratory coordinate system. Given our objective and the assumption that the beam within the setup is simple astigmatic, we overlooked the angles, as they remain constant along the optical axis for simple astigmatic beams. While the angles across small parts (or regions) of the setup are quite consistent, overall there is some rotational movement observed in the angles for the major and minor axes of the beam. These could be attributed to the presence of various interference fringes, which may affect the fitting accuracy. However, this explanation seems quite unlikely. We have plotted in figure 4.16 the angle estimates ($\phi$) derived from the reference beam measurements for part 1. An abrupt change in angle, observed around 300 mm along the optical axis, is attributed to a shift in the beam's major and minor axes, and is in-line with our expectations. Apart from this, there is a gradual and steady change in the values, which suggests the axes of the beam is rotating along the optical path, and the beam in the setup might be general astigmatic as elaborated in section 2.4.

While modeling the reference beam setup, we did not account for the beam's propagation through the optical single mode fiber. However, understanding the coupling of the beam with the optical fiber is important. We have experienced significant power losses in the fiber. The input power of the beam entering the collimator is approximately 82 mW, but the highest output power achieved through rigorous alignment was only 25 mW. Typically, the output power has been observed to be around 3-4 mW, resulting in a substantial 96.34% loss of power in the fiber. The observed power losses are mainly due to the beam's misalignment with the fiber. A mismatch between the beam size and the fiber's mode field diameter could also contribute to these losses. Ideally, maximizing the output power is desirable for the efficiency of the system. Although, in our case, the low power values do not impact the phase measurements.

# 5

# Phase Measurements

The working principle of the phase camera is outlined in Chapter 3. To recap, we conduct static phase measurements of the heterodyne beat signal, which is 80 MHz, without any sideband (phase-modulated) frequencies. In this chapter, we will primarily focus on the phase measurements performed using the PC, and the various noise sources (phase noise) that lead to drifts in the setup, or equivalently, fluctuations in the phase measurements. Our overall goal is to improve the measured phase resolution. Therefore, we have conducted various measurements to identify the phase noise sources and have made efforts to eliminate them. Towards the end of this chapter, we will demonstrate the overall improvement in phase resolution and the reduction in phase noise floor.

Our discussion begins with an analysis of the actual phase measurements. Using the current setup, several phase measurements were recorded and analyzed at different timestamps. Each single frame of the measurement consists of 16,384 phase measurements. The measurement time for each frame is 0.537 s. This was explained in section 3.2.2. One of the very first measurements is depicted in figure 5.1, which represents 100 (100 $\times$ 16,384) successive unwrapped phase measurements. Over a time period of a few hundreds of seconds, substantial fluctuations in the measured phase are evident. Specifically, the phase changed from approximately 1.67$\pi$ rad to nearly 2.32$\pi$ rad, amounting to a shift of about 0.65$\pi$ rad. The sub-figures 5.2a - 5.2d, provide a more detailed view of single phase measurements (1 $\times$ 16,384). All of these frames display random, yet discernible, patterns of fluctuations. For example, figure 5.2a shows scattered phase values without a clear trend, while figure 5.2b shows an oscillation ($\sim$ 2 Hz) around a mean value, typically characterized by a periodic or cyclical (sinusoidal) pattern. From these observations, we can define two types of stability for the setup: long time-scale stability, measured over several hundreds of seconds, and short time-scale stability, measured over a few hundred milliseconds. Each type of stability is influenced by different noise sources and its nature, which will be discussed in detail when we explore phase noise later in this chapter. For the purposes of this work, our primary interest lies in the short-time scale fluctuations in phase, which attributes to the phase resolution.

Phase resolution in our setup refers to the small-time scale fluctuations observed in the phase measurements. It essentially denotes the smallest fluctuation in phase that the PC can reliably and consistently detect. Principally, these fluctuations can never be zero due to inherent detector or thermal noise from the amplifiers in the photodiode. Although thermal noise represents the fundamental limit of the detector, phase resolution is also influenced by several other factors that may dominate over thermal noise. This includes the stability of the environment in which the measurement is conducted.

Figure 5.3 illustrates short time-scale fluctuations (approximately 130 ms) of the phase measurements. This figure captures the first 4000 phase data points from the single measurement frame shown in figure 5.2a. To determine the resolution, we fit a linear function to the measurements that is used to subtract the slow phase changes (fluctuations). The linear fit along with the histogram of the difference between the data points and the linear fit is shown in the figure 5.4. The standard deviation ($\sigma$) of these differences represents the measured phase resolution of the system. For the measurement

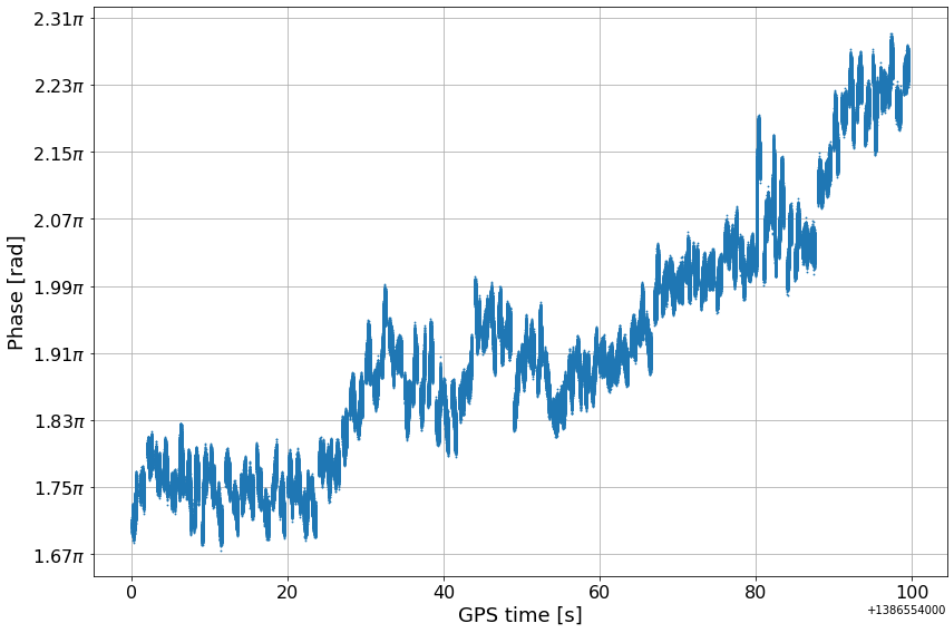


**Figure 5.1:** 100 (100 × 16,384) successive frames of the phase measurements performed using the PC. Each measurement cycle lasts 1 s, during which the phase is measured for the first 0.537 s, and the system remains idle for the remainder. The time is represented in GPS format.

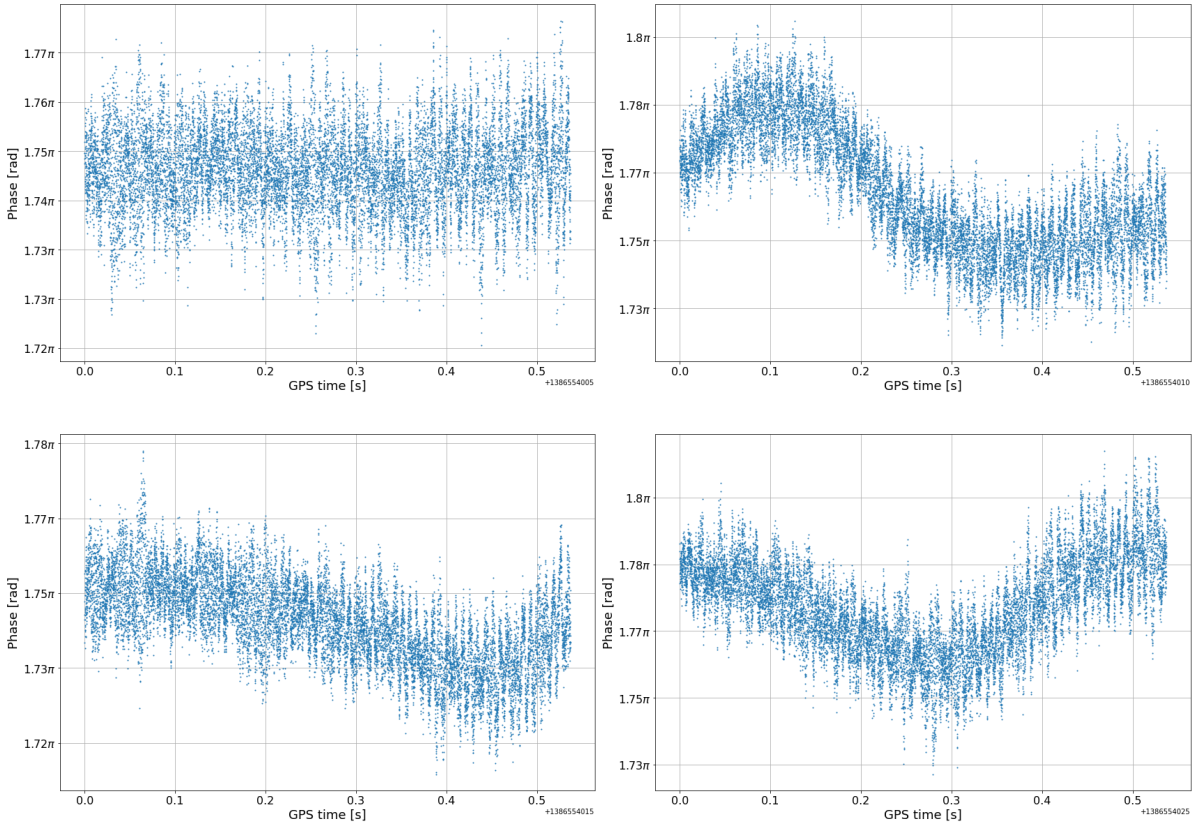


**Figure 5.2:** Single phase measurements recorded at different GPS timestamps, which are represented on the bottom right of each plot.

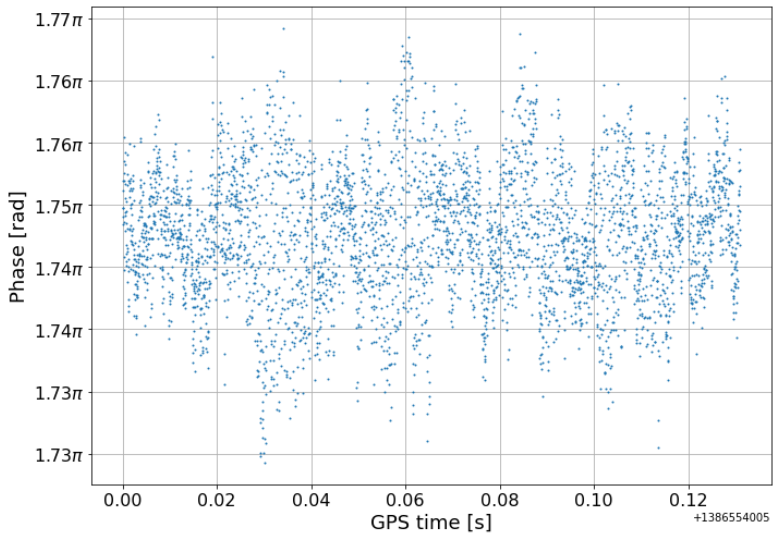


**Figure 5.3:** The observed fluctuations in the first 130 milliseconds (short-time scale) of the phase measurements.

exemplified, the phase resolution is 20.80 mrad. We will more formally and systematically compute the phase resolution of our system for all the various measurements performed at different timestamps, in section 5.3. For the time being an initial estimate and understanding of the measured phase resolution is sufficient.

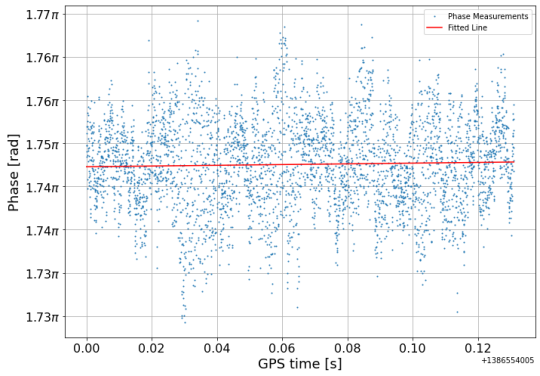


**(a)** Linear fit of the phase measurements shown in figure 5.3.

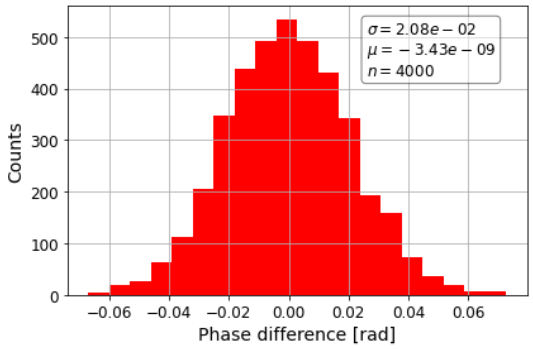


**(b)** A histogram of the difference between the linear fit and the phase measurements. $\sigma$ represents the phase resolution.

**Figure 5.4:** The phase resolution of the measurement.

At the outset, we expressed our goal to improve the phase resolution. The pressing questions now are: what causes these fluctuations, and how can they be determined & reduced? We will begin by addressing the causes of these fluctuations.

## 5.1. Phase Noise

The sensitivity of interferometers to displacement of its optical elements is rooted in the fundamental principles of the instrument. Such an instrument which is dedicated to measure optical beam paths or wavefronts with high resolution, always runs the risk of being disturbed by its environmental conditions [20]. Various sources of error and environmental factors reduce the stability and reliability of the interferometric phase measurements, collectively referred to as phase noise or simply noise in this work. In this context, noise generally denotes random errors that derive from electrical, optical, mechanical or environmental sources and that behave in a statistical way such that their determination is not possible [20].

### 5.1.1. Error Sources

In a complex optical setup there are various sources of noise that are inherently present (or coupled) in the system [20, 21, 22, 23, 24, 25]:

1. Electronic noise, including shot noise, readout noise, and noise from electronic manipulators like AOMs or EOMs.
2. Laser frequency noise and beam jitter.
3. Environmental fluctuations, such as mechanical and acoustic vibrations (from machines, human activity, electronic devices, etc.), temperature changes, air turbulence, radiation from various sources, seismic activities, and more.
4. Misalignment and changes in the shapes of interfering beams.
5. Speckle effects caused by rough or unclean optical surfaces, and ghost beams.

Depending on the noise sources and their frequencies, the phase measurements and optical wavefronts are affected in different physical ways. For example, thermal stability, and convection, can alter the refractive index of the air through which the beam propagates, thereby affecting the wavefronts and the optical path length (OPL) traveled by the beam. Temperature changes also affect the refractive index, focal length and the geometry of the optical components. Similarly, mechanical vibrations can cause physical displacements of the optical components, such as mirrors and lenses, mounted on the bench. This leads to changes in the OPL and consequently affects the phase and other properties, such as the RoC of the wavefronts, which are all inherently coupled. Acoustic noises can also generate vibrations or pressure waves that subtly change the OPL. Acoustic vibrations mainly have two different effects on an optical setup [20]:

- The propagation of sound waves through air causes local regions of compression and rarefaction. The compressed and rarefied air causes a direct change in the OPL depending on the sound level of and the distance from the source.
- Acoustic vibrations can also cause mechanical setups to vibrate. The magnitude of this excitation depends on the resonance frequency and the damping characteristics of the structure or design. This effect becomes particularly relevant when the setup's or component's (mounts) eigenfrequency coincides with a strong spectral acoustic component, potentially causing it to resonate.

Until now, we have primarily focused on the sources of noise and less on their frequencies. Our main interest lies in phase resolution, which directs our attention to studying noise at higher frequencies. Consider an example where something in the external environment changes at a frequency of about 1 Hz or even lower. Noise at these frequencies do affect the phase measurements but since the measurement time is 0.537 s and given that we are interested in internal changes in the wavefronts, only high frequency noise are of interest to us. If an optical component vibrates at 2 kHz, these rapid changes directly impact the phase measurements, manifesting as fluctuations. In this work, fluctuations above 10-20 Hz are considered high-frequency. It is also worth noting that low-frequency noise sources impact the long-term stability of the setup. The fluctuations observed in figure 5.1 over 100 seconds predominantly correspond to low-frequency fluctuations, which lead to significant changes in the measured phase of the wavefronts.

With this construct, we have established the key relationship between interferometric measurements and its working environment. Now, before elaborating on the actual phase noise sources present in the prototype PC setup, we will briefly explain the coupling between these noise sources and the interferometer setup. This overview will help provide a better understanding and a physical sense of the changes involved.

### 5.1.2. Coupling

Building on the phase noise, one may wonder how it gets coupled to the interferometer or the phase measurements. Consider a simple scenario of two laser beams, with optical intensities $I_1$ and $I_2$, originating from the same laser source. The interference of these two beams is then given by the equation:

$$I(t) = I_1 + I_2 + 2\sqrt{I_1 I_2}\cos\left(2\pi f_m t + \phi(t)\right) \tag{5.1}$$

where $f_m$ is the modulation radio frequency of 80 MHz. With the phase measurement, we measure $\phi(t)$, which represents the phase difference between the reference beam ($\phi_{ref}$) and test beam ($\phi_t$) in our setup.

$$\phi(t) = \phi_{ref} - \phi_t \tag{5.2}$$

For a simple stigmatic Gaussian beam, the phase term incorporates the Guoy phase, wavefront curvature, and the OPL, as given by equation 2.8. Therefore for the interference of two simple Gaussian beams, the phase difference, $\phi(t)$, is given by [4]:

$$\phi(t) = \Delta R - \Delta G + \Delta L \tag{5.3}$$

where the wavefront curvature difference, $\Delta R$, of the interfering beams is $k(x^2+y^2)/R_r - k(x^2+y^2)/R_t$, with $R_r$ and $R_t$ representing the radii of curvature of the wavefronts of the reference and test beams, respectively. $\Delta G$ represents the Guoy phase difference, and $\Delta L = k(l_r - l_t)$ represents the optical path length difference (OPD) between the two beams, with $l_r$ and $l_t$ representing the OPL travelled by the reference and test beams in the arms, respectively. To a very good approximation, we can neglect the Guoy phase and wavefront curvature term, i.e. we are making a plane wave approximation for our beams. In such a case, $\phi(t)$ is simply equal to $\Delta L$. Since the beam is equally split into two arms, we can assume that the initial phase difference between the beams is zero. Therefore, $\phi_{ref}$ and $\phi_t$ solely depend on the path lengths traveled by the beams in their respective arms. So for a laser beam of wavelength 1064 nm, a phase resolution of 20 mrad, corresponds to an OPL fluctuation of approximately 3.4 nm, under the plane wave assumption.

To further explain how phase changes or fluctuates, let's consider mechanical vibrations as the primary source of noise. Lets assume that one (only one) of the mirrors in our setup vibrates sinusoidally with a frequency $f_{vib}$ along the beam path, and a very small amplitude A. We treat these vibrations as noise. As the mirror's vibrations alter the OPL, they result in variations in the phase difference measured at the photodiode. In such a scenario, the phase difference between the two beams can be expressed as follows [26]:

$$\phi(t) = \phi_o - \frac{2\pi}{\lambda} A \cos\left(2\pi f_{vib} t + \phi\right) \tag{5.4}$$

where $\phi_o$ represents the phase difference of the two beams given by equation 5.2, and $\phi$ represents the phase of the vibration. $\phi_o$ is the slowly varying phase term which accounts for any arbitrary optical phase variations between the two arms, excluding those caused by vibrations. In the presence of a vibrating mirror or surface, the interference (or cross) term of the equation 5.1 can be modified to account for the impact of vibrations and is given by [26]:

$$I_{12} = 2\sqrt{I_1 I_2}\left[\cos\left(2\pi f_m t + \phi_o\right) + \frac{2\pi A}{\lambda}(\cos[2\pi(f_m + f_{vib})t + \phi + \phi_o] - \cos[2\pi(f_m - f_{vib})t - \phi + \phi_o])\right] \tag{5.5}$$

Equation 5.5 shows that the vibration of the mirror leads to phase modulation of one of the beams. The interference term gives rise to modulated sideband frequencies at $f_m \pm f_{vib}$. Analyzing the frequency spectrum of the photodetector signal would reveal modulation peaks, as depicted in figure 5.5. These sidebands are created due to the vibration-induced phase modulation of the beam. The additional modulation term in equation 5.4 contributes to fluctuations in the measured phase and depends significantly on the amplitude of these vibrations.

We have now established that the phase of the measured beat signal is related to the OPD traveled by the beams in the arms of the interferometer. Consequently, the fluctuations observed in phase measurements, as shown in figure 5.2, can be partly correlated to fluctuations in OPL over time. Changes in OPL can be induced by any noise sources as discussed in the previous section 5.1.1. In an ideal scenario where an interferometer setup is assumed to be completely static and isolated, it is expected that relative phase measurements of laser beam wavefronts would consistently yield a constant value with zero fluctuations.

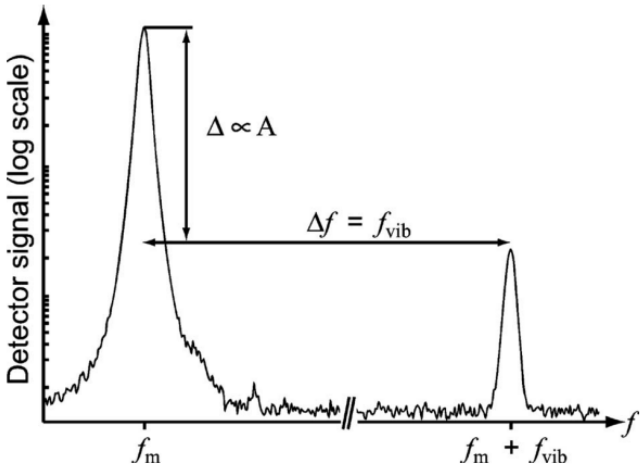


**Figure 5.5:** Frequency spectrum of a vibration induced phase modulation [26].

## 5.2. Investigation of Phase Noise

To analyze the spectral components leading to phase fluctuations, we examine the power spectral density (PSD) of the time-domain phase measurements. The frequency spectrum provides an informative and intuitive view, allowing us to identify the frequencies of the noise sources. The root-mean-square (RMS) PSD of one of the initial measurements is shown in figure 5.6, calculated by averaging over 100 single measurement frames. The x-axis of the plot represents the frequency range up to the Nyquist frequency, which is 15.45 kHz, while the y-axis shows the distribution of power across different frequency components of the signal, measured in $Rad^2/Hz$. In this study, we focus primarily on the dominant phase noise sources. Based on initial studies of the frequency spectrum of different measurements, we identified the main spectral noise components. These frequencies, observed in almost all the initial phase measurements, include 120 Hz, 200-700 Hz, 1.35-1.38 kHz, 1.8 kHz, 2.3-2.8 kHz, and 3.3 kHz.

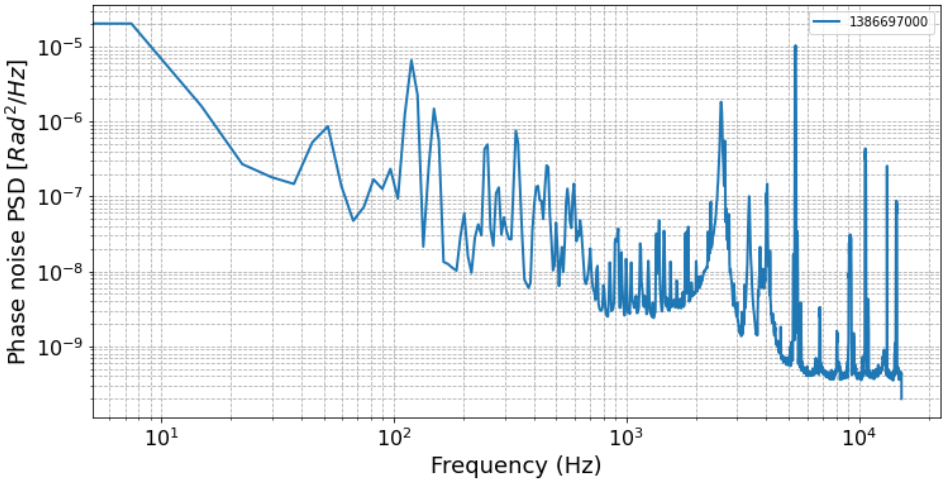


**Figure 5.6:** Root-mean square phase noise power spectral density of the phase measurements, obtained by averaging 100 single measurement frames.

The PSD of our frequency range of interest, with some dominant frequencies highlighted, is displayed in figure 5.7. In this figure, we can observe spikes at certain frequencies, indicating narrow bandwidth noise signals. These spikes indicate discrete frequency components where phase noise is concentrated. It is observed particularly between 1000-2000 Hz, as seen in the plot. These frequencies may be related to acoustic noise present in the lab, and could represent harmonics or interference at specific frequencies. On the other hand, broadband peaks on the graph indicate areas where phase

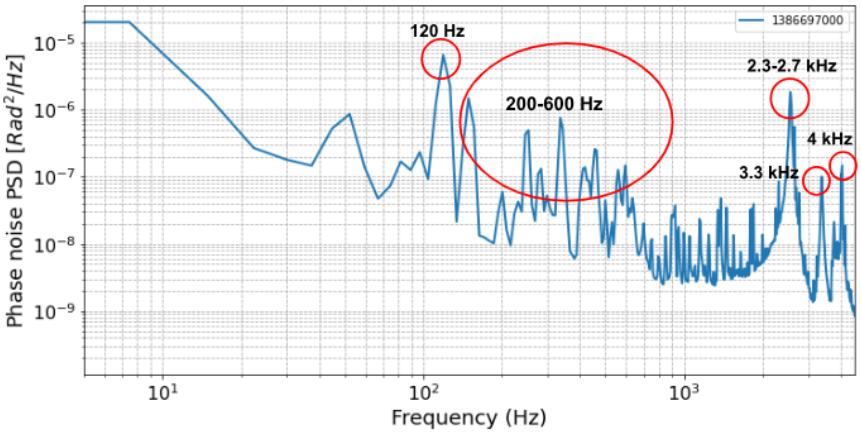


**Figure 5.7:** Phase noise PSD with dominant noise frequencies highlighted.

noise power is elevated over a broader range of frequencies, rather than at discrete points. In the plot, this is particularly evident in the frequency ranges of 2.3-2.7 kHz, 3.3 kHz, and 200-600 Hz. These peaks can be caused by sources that vibrate or resonate across a range of frequencies, indicative of a low quality factor or Q-factor, and can be related to mechanical vibrations of optical components. Multiple elements within the setup may contribute to a complex pattern of phase noise due to their resonant behaviors. Another important parameter that we can deduce from the PSD plots is the jitter or RMS phase noise, which represents the integrated phase noise. The jitter gives us an indication of the total phase noise (in mrad) present in the phase measurements. A plot representing the PSD of one of the phase measurements, along with the computed jitter, is shown in figure 5.8. The cut-off frequency for the calculations is 10 Hz. We are only interested in the total jitter value, which is 25 mrad as indicated in the plot.

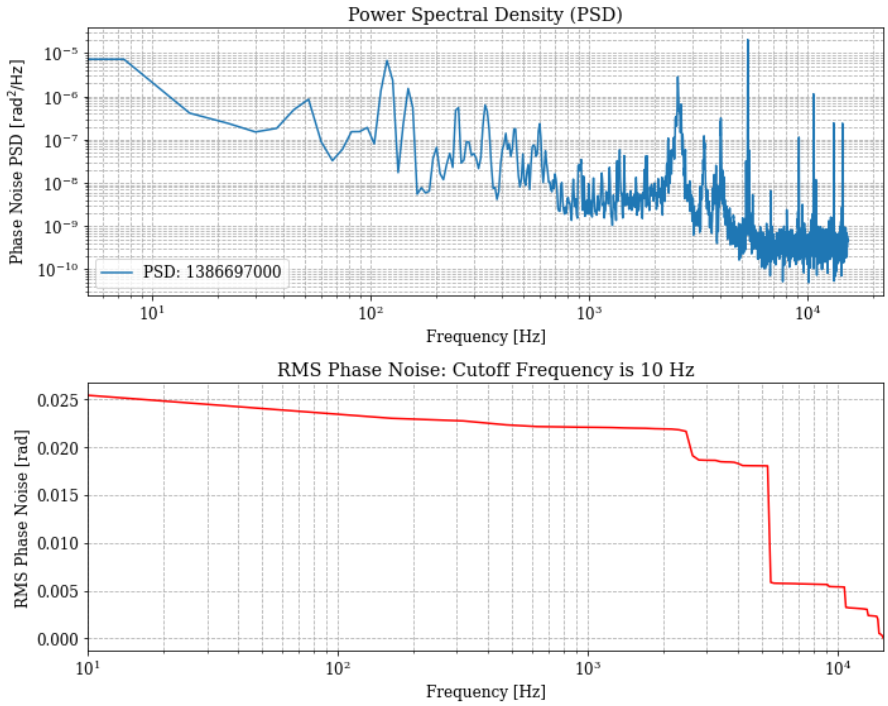


**Figure 5.8:** PSD and the computed RMS phase noise (jitter) from one of the initial phase measurements.

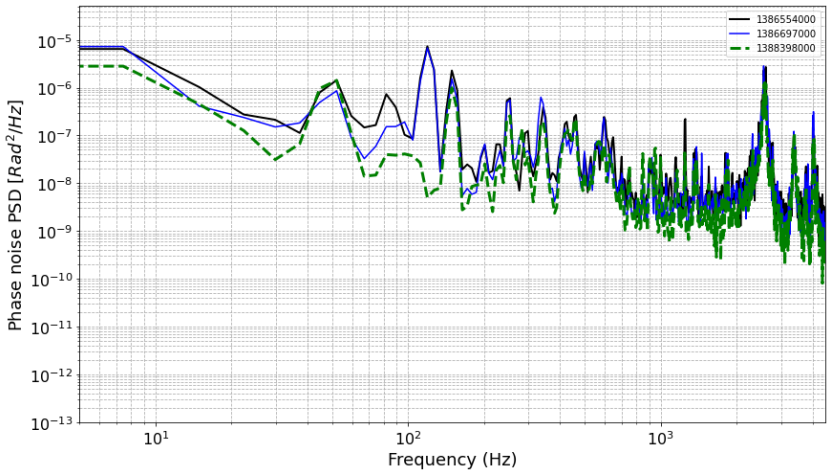


**Figure 5.9:** Comparison of phase noise PSD across different measurements. The green plot represents the PSD after alignment correction, portraying no phase noise at 120 Hz.

Interestingly, while we now have information about the frequencies of the noise sources, we have yet to identify the sources themselves. Nevertheless, this initial analysis is sufficient for us to adopt a derivative and investigative approach to correlate these noise frequencies with their possible sources through additional measurements. For example, the 120 Hz peak shown in figure 5.7 was quickly linked to the scanner. By properly aligning the beam with the scanner, we were able to eliminate the noise source from the measurements. It was determined that misalignment and clipping of the beam at the scanner had been causing the phase noise at 120 Hz. For reference, figure 5.9 plots the PSD of several initial recorded phase measurements. The dotted line (green) represents the phase measurements after alignment correction, showing no peak at 120 Hz. Overall, all initial measurements share the same dominant phase noise spectral components.

To identify the sources of other phase noise, we conducted various measurements using accelerometers, geophones, microphones, and quadrant photodiodes (QPDs). These tools helped us study different sources of noise in the lab environment, including seismic, acoustic, and vibrational disturbances. In the upcoming sections, we will elaborate on the measurement results using these tools, and attempt to correlate them with each other and with the phase noise PSD.

### 5.2.1. Vibrational Stability of the Setup

We studied the vibrational stability of the optical setup, including the bench and its components, using geophones and accelerometers. These devices measure acceleration or velocity and are capable of detecting and measuring vibrations or seismic activities. Specifically, we used geophones to monitor vibrations of the bench from environmental disturbances. Accelerometers were employed to measure the acceleration or displacement across all three axes of various optical mounts and components on the bench. Our focus is to analyze the spectra of these measurements to identify the frequencies at which the components are vibrating. We will then correlate these frequencies with those observed in the phase noise PSD, as shown in figure 5.7.

#### Accelerometer Measurements

We connected the output of the piezoelectric accelerometer (Brüel & Kjær DeltaTron Accelerometer Type 4508-B-002) to an FFT Analyzer (Ono Sokki CF-9200), which provided the amplitude spectral density (ASD) measured in $V_{RMS}/\sqrt{Hz}$. Since our primary interest is in displacement, we converted the units of the ASD to $m/\sqrt{Hz}$. The conversion factor of the accelerometer is 100.4 mV/($m/s^2$). The frequency range of the accelerometer is 0.4 Hz - 8 kHz. It's important to note that the axes (or planes) of the mounts may differ from the beam axis or laboratory coordinate system due to the orientation of the mirrors ($\sim 45°$) relative to the beam. This is clearly visible in the optical setup shown in figure 3.2. Measurements with accelerometers were conducted along the planes of the component, not the beam axes. So only a component of the displacement along the beam path leads to the changes in

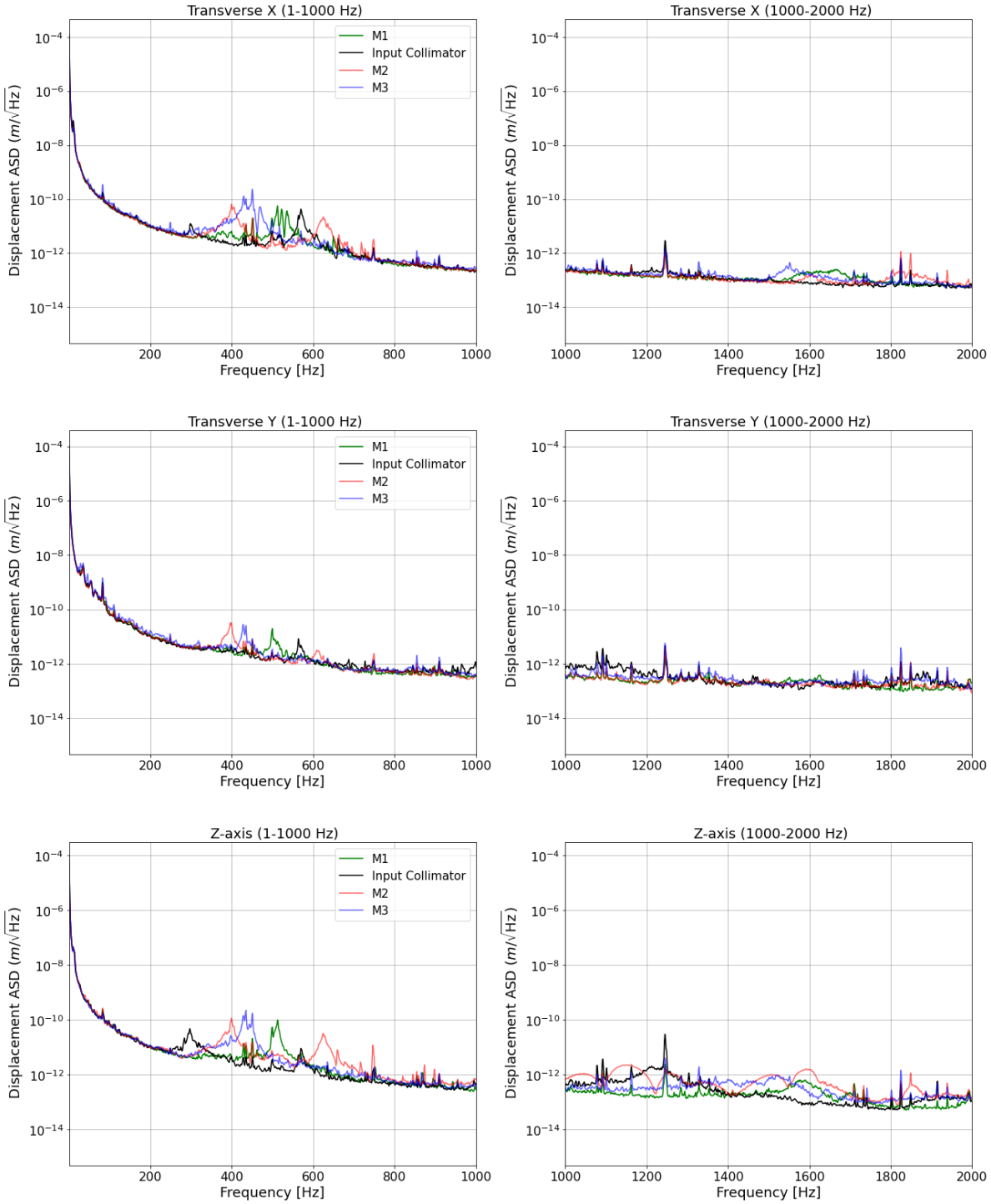


**Figure 5.10:** Results (1/2) of the accelerometer measurements, performed on various optical mounts along all three axes.

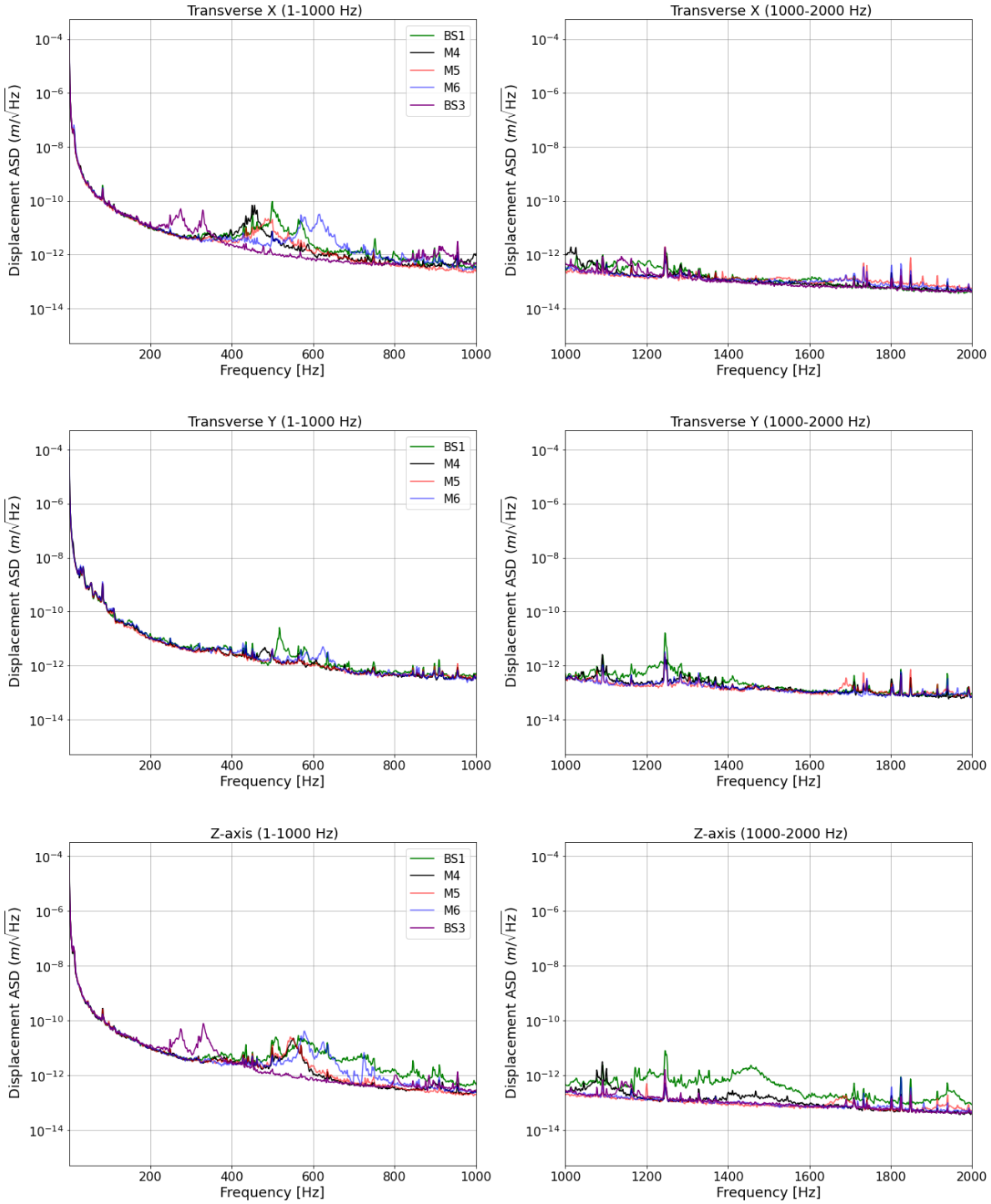


**Figure 5.11:** Results (2/2) of the accelerometer measurements, performed on various optical mounts along all three axes.

OPL. Since many of the mounts and components in the setup are similar, we grouped them to study their measurements. Figures 5.10 and 5.11 show the displacement ASD for the mounts of various optical components, with annotations consistent with the PC setup depicted in the figure 3.2. Our analysis focuses on the frequency range of 20-2000 Hz, which leads to major fluctuations. The displacement, measured in m/$\sqrt{\text{Hz}}$, generally decreases as the frequency increases, which is a common behavior as higher frequencies often have less energy. Higher frequencies often show lower values because the energy per frequency (bandwidth) unit decreases. This is also partly because energy sources (like mechanical drives, or seismic activity) often have energy spectra that decrease with frequency. Hence, less energy is available to excite the system at higher frequencies, resulting in smaller displacements. Notably, the broadband displacement for mirror mounts and beam splitters (M1, M2, etc.) predominantly exist within the 200-700 Hz range. Each mount resonates at a unique frequency consistent across all three axes, suggesting these peaks correspond to the mechanical resonances of the mounts, with a low Q-factor. Figure 5.12 illustrates the resonance frequencies of various optical mounts for reference. An initial study suggests these resonance frequencies typically fall within 200 Hz to a few kHz range and vary depending on several factors such as material, mounting structure, clamping method, and damping design [27, 28]. For example, clamping the same mount to the bench in a different way can lead to a change in its resonance frequency, as illustrated in figure 5.13.

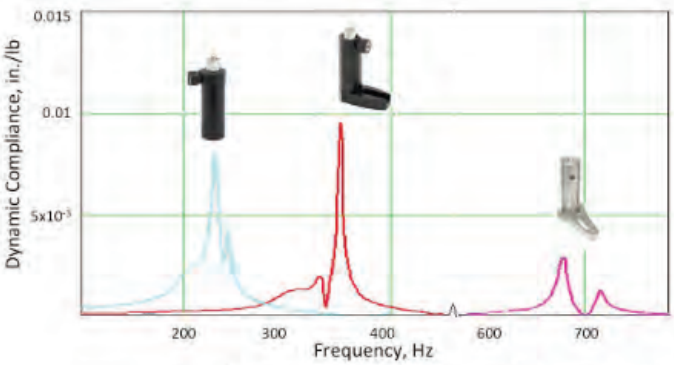


| | STANDARD POST | SLOTTED BASE | PEDESTAL POST |
|---|---|---|---|
| RESONANT FREQUENCY PEAK | 250 HZ | 350 HZ | 680 HZ |
| COMPLIANCE | 0.0070 IN./LB | 0.0095 IN./LB | 0.0043 IN./LB |

**Figure 5.12:** Resonance frequencies of different mounts from Newport [28].

Apart from these resonances (or vibrations), there are several other noise frequencies. Particularly, 83 Hz, which is consistent across all measurement axes. The transverse Y-axis shows the maximum displacement at this frequency, suggesting that the bench might be resonating vertically. Additionally, narrowband displacement noise is more prominent in the frequency range of 1000-2000 Hz, with specific frequencies at 1.25 kHz, 1.82 kHz, and several others. Given the nature of these peaks, they likely represent acoustic noise and its harmonics. This was observed when we performed measurements by introducing noise, using an audio noise generator, at a known frequency using a to observe its effects on the accelerometer measurements. Indeed, we observed a sharp peak along with multiple harmonics of the induced noise.

To illustrate the RMS displacement (similar to jitter), which represents the integrated displacement, across different frequency bands, consider the ASD of M3 for the z-axis, as shown in figure 5.10. The RMS displacement over the entire spectrum of 20-8000 Hz is approximately 7.67 nm. Similarly, for the resonance peaks (200-700 Hz) it is about 0.62 nm, while the displacement contribution beyond 700 Hz drops to just 15-20 pm. Thus, the main displacement noise contribution predominantly arises from lower frequencies, particularly below 100 Hz. Comparing this RMS displacement from one of the initial phase measurements shown in figure 5.8, the total jitter is about 6.3 mrad for 200-700 Hz frequency

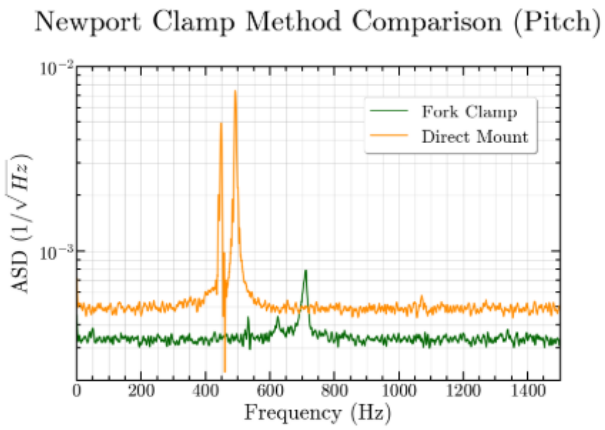


**Figure 5.13:** The affect of clamping on the resonance frequencies of the optical mounts [27].

range. This corresponds to optical path length fluctuations of about 1.05 nm. Given that a component of the displacement (0.62 nm) contributes to actual path length fluctuations, and considering the complexity associated with the simultaneous 3D displacement of all the components, these results are reasonably compatible.

We will now discuss the accelerometer measurements of the scanner, performed with and without its electrical actuation (static). This comparative analysis is shown in figure 5.14. It is clear that when the scanner is actuated, displacement ($m/\sqrt{Hz}$) increases, particularly in the frequency range beyond 1500 Hz, considerably across all three axes. This increase in displacement is mainly due to the scanner vibrating or resonating at 2.3-2.7 kHz along the transverse planes, and at 3.3 kHz along the beam path (z-axis), when actuated. It could be the white electronic noise of the scanner responsible for the resonances at these frequencies. For frequencies below 1500 Hz, the ASD is almost identical for both sets of measurements, indicating that any noise in this regime corresponds to the mechanical structure of the scanner. Even without the actuation, we see the mechanical structure of the scanner vibrating at about 2700 Hz and 400 Hz in the transverse X axis. Additionally, the 83 Hz peak is also prominent in the transverse Y axis.

Correlating these findings with the phase measurements, the phase noise PSD, as shown in figure 5.7, also indicates dominant phase noise at 200-700 Hz, 2.3-2.7 kHz, and 3.3 kHz. These are likely originating from the mechanical vibrations and resonances of the optical mounts and the scanner on the bench. The frequency of narrowband displacement noise discussed in this section are also evident in the phase noise spectra. Identifying the resonance frequency or vibration of various components has helped us pinpoint the major noise sources affecting the phase measurements.

### Geophone Measurements

We used a geophone (Sercel L4C) to study the vibrations of the bench, focusing specifically on the frequency domain. The optical setup shown in figure 3.3 defines the planes or coordinate axes of the bench. This analysis was complemented by accelerometer measurements, which also highlighted vibrations, particularly in the low-frequency range of 0-25 Hz and at 83 Hz. These vibrations were primarily observed in the transverse directions (x & y) of the bench. Figure 5.15 shows the Fourier transform of the geophone time-domain measurements, illustrating the frequency domain of the vibrations. These vibrations might be induced by air flow, the ventilation system, acoustic noise, and other environmental factors. The longitudinal axis (z-axis) did not show prominent vibrations at lower frequencies, however accelerometer measurements indicated some vibrations at higher frequencies beyond 800 Hz. However, due to their low amplitude, these higher frequency vibrations were not considered significant for this study.

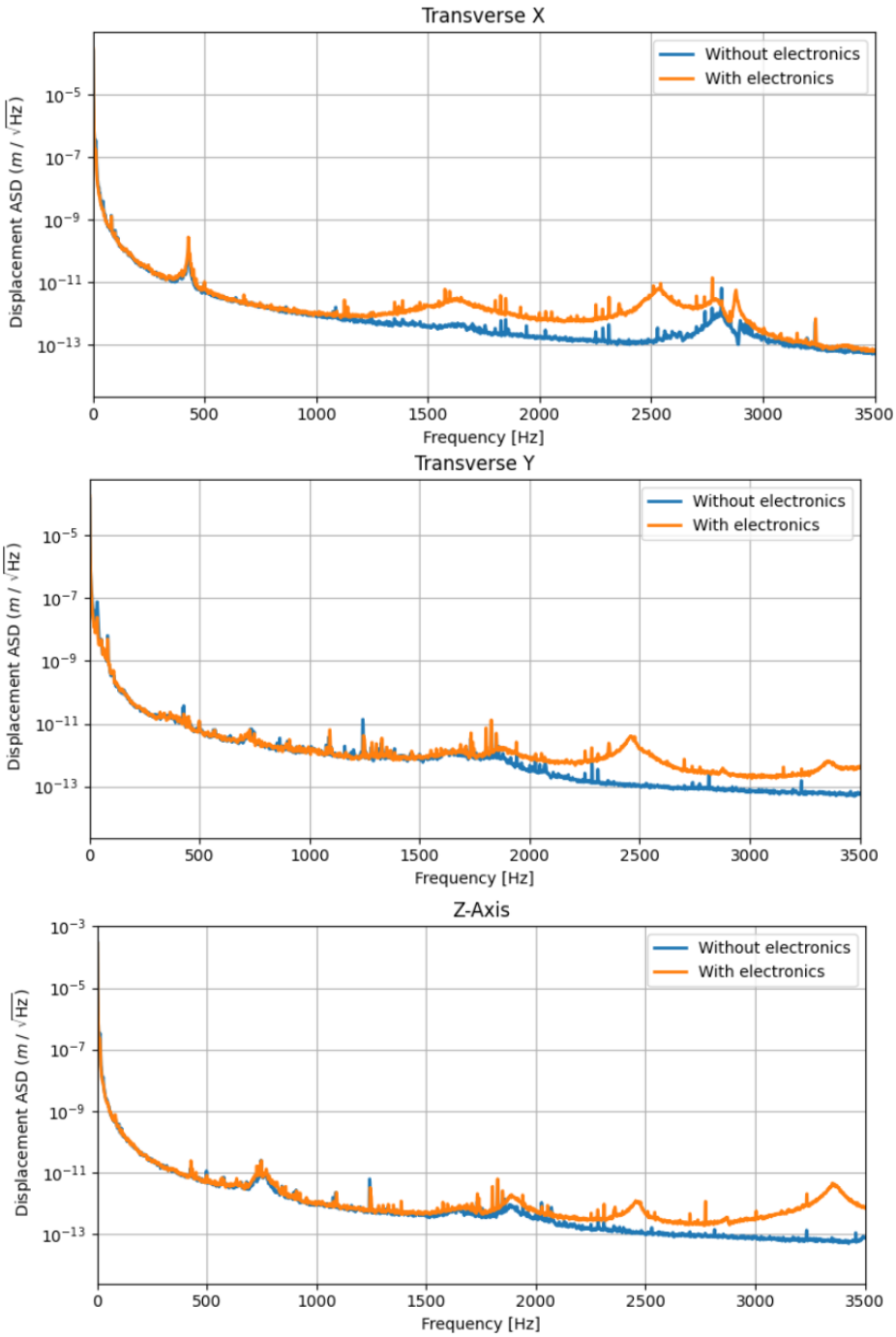


**Figure 5.14:** Results of the accelerometer measurements performed on the scanner.

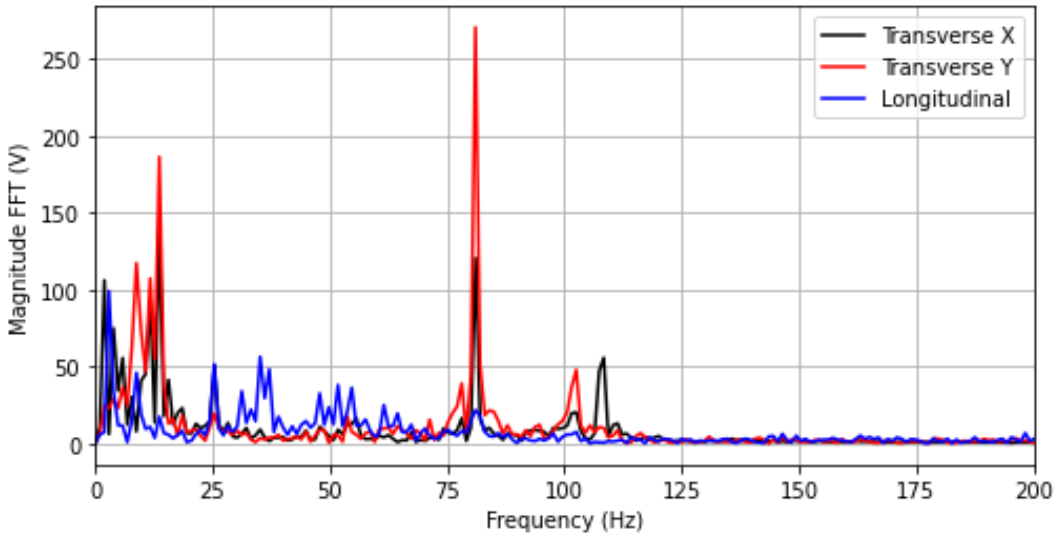


**Figure 5.15:** Frequency spectrum of the geophone time domain measurements.

### 5.2.2. Acoustic Noise

To study the acoustic noise present in the optical lab, we used a microphone (NTi Audio M2230). Acoustic noise can originate from various sources; computers, data acquisition systems (DAQs), CPUs, heating, ventilation, and air conditioning (HVAC) systems, among others. Our objective was to determine the frequencies of these noise sources. We also tried to determine the source of the acoustic noise, but could not clearly pin-point the source. The coupling of acoustic noise to the interferometer has been previously described in 5.1.1. In this section, we will briefly discuss the measurement results.

Using the microphone, several measurements were recorded in the lab across different frequency bands, as plotted in figure 5.16. For low-frequency noise, ranging from 7-1700 Hz as seen in figures 5.16a and 5.16b, there is a dominant peak at 83 Hz of similar intensities in both measurements. Additionally, a sharp acoustic noise at 1250 Hz is observed. For higher acoustic frequencies, as displayed in figure 5.16c, there are notable broad peaks around 3-3.2 kHz and also at approximately 8.2 kHz. Acoustic noise at these aforementioned frequencies can cause the mounts, scanner, and optical bench to resonate. Notably, the sharp acoustic noise around 3 kHz and even the harmonics of 1250 Hz could induce resonance in the scanner. We also observed that the 83 Hz acoustic noise leads to vibrations in the bench and optical mounts, as discussed in preceding section. The frequencies of these noise are also visibly present in our actual phase measurements. Overall, all of these findings are quite consistent with other measurements that we have performed.

### 5.2.3. Laser Stability Measurements

In our prototype PC setup at Nikhef, we frequently observed misalignments of the optics over extended periods, typically 4-5 weeks. Especially, the input beam of the AOM (or input collimator) is very sensitive to misalignments. This issue could be attributed to the poor long-term pointing stability of the laser beam. Since the beam entering the PC setup is preconditioned and traverses through numerous optical components and undergoes several transformations, there could be one or multiple reasons for the observed laser pointing stability issues. There are various reasons which can cause this - thermal deformation or sagging of the optics, environmental vibration, etc. Our initial approach to resolve this issue was to measure laser stability at various positions within the setup. Please do note that these measurements were not performed on the PC setup, but instead in the pre-conditioning part of the optical setup. Since this part incorporates the common optical path of the laser beam (before the splitting), direct correlation to the phase measurements and phase noise does not make sense. However, this study will still provide insights into the pointing stability of our laser beam. We will briefly discuss one of the measurement results and comment on the pointing stability of the laser beam.

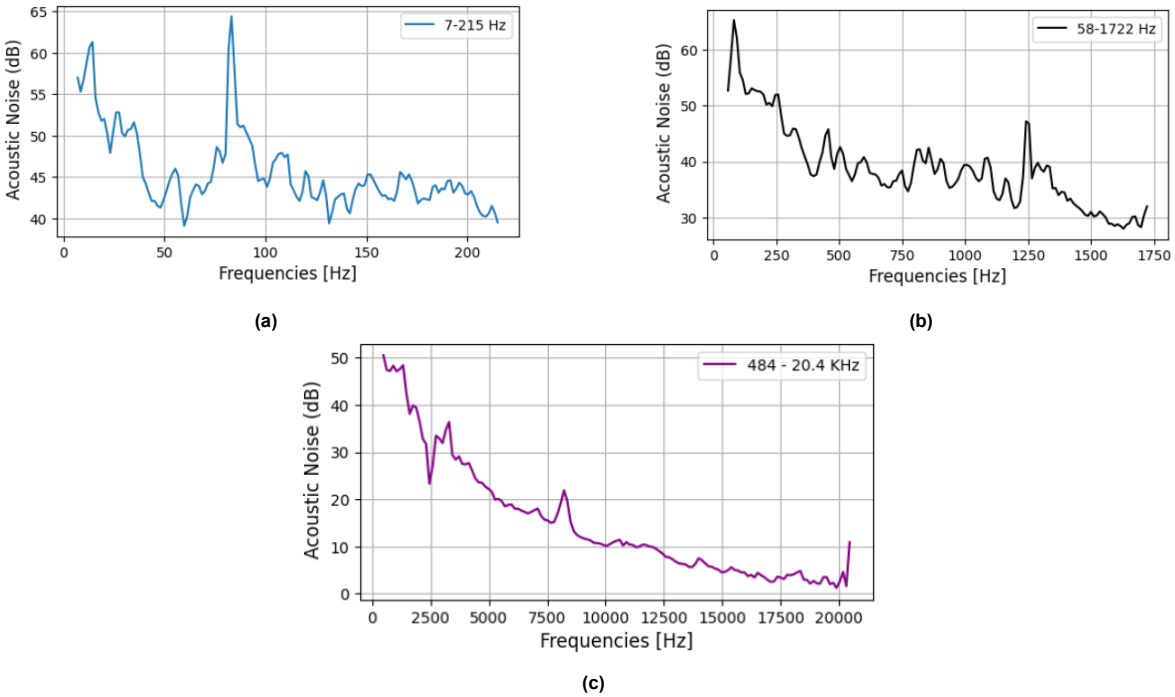


**Figure 5.16:** Measurements of the acoustic noise, at different frequency bands, present in the optical lab environment.

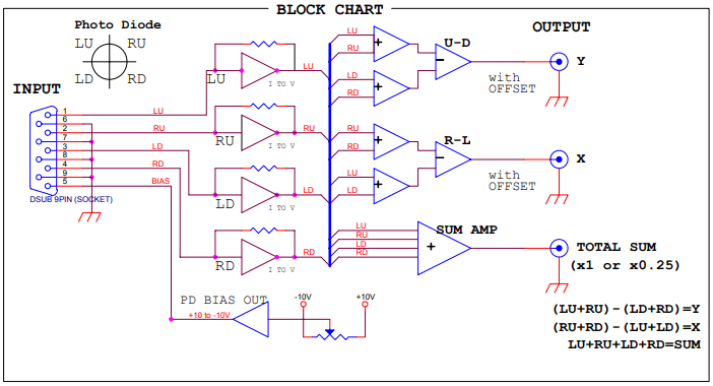


**Figure 5.17:** Block diagram of the QPD amplifier [29].

To analyze the spatial stability of the laser beam, we placed a Quadrant Photodiode Amplifier (GNA 190, T4) in the beam path. The quadrant photodiode (QPD) employed is an Si PIN Photodiode (Hamamatsu, S5980). The segmented nature of the QPD allows for analysis of the optical signal from all four quadrants; converting the intensity of light falling on each quadrant into equivalent electrical (current) signals. The conversion from current signals to voltage can be chosen by adjusting the transimpedance; for our experiments, it was set at 10 V/mA. The block chart for the QPD Amplifier is represented in figure 5.17. Mathematically, the output of the QPD amplifier is designed to provide the difference between both halves and the overall sum of the signals from all quadrants, as follows:

$$X = (RU + RD) - (LU + LD)$$
$$Y = (LU + RU) - (LD + RD)$$
$$S = LU + RU + RD + LD$$

.

Here, X and Y represent the differential signals corresponding to the horizontal and vertical displacements of the beam, respectively, while S indicates the total light intensity captured by the QPD. The

variables RU, RD, LU, and LD denote the light intensity in the respective quadrants, as marked in figure 5.17. The three outputs of the QPD are connected to an FFT Analyzer (Ono Sokki CF-9200). With the analyzer, we measured over a period of 24 hours. To observe laser movement trends over 2-3 days, we conducted multiple continuous 24-hour measurements.

It would be beneficial to mention here some other intricacies and dependencies related to these stability measurements. The size of the beam impinging on the QPD is crucial for sensitivity to beam displacements. A smaller beam concentrates light intensity over a smaller area, resulting in higher local intensity variations for spatial movements – producing stronger signals in response to minute positional changes of the beam. With this consideration, the beam size was converged to approximately 500-600 $\mu m$ in diameter using convex lenses of varying focal lengths. This size was ideal relative to the dimensions of the QPD and also facilitated easier alignment. During most of these measurements, the beam was precisely centered, achieving nearly equal intensity of light falling on each of the QPD's quadrants, such that X = 0 and Y = 0.

Another important aspect to consider is the responsivity ($\mathrm{A\,W^{-1}}$), of the Silicon sensor of the QPD at 1064 nm spectral wavelength. The responsivity based on the specification sheet of the QPD is approximately 0.35 A/W [30]. Although, we conducted rough calculations based on the actual beam measurements and experimental parameters. The total power impinging on the QPD is approximately 167 $\mu$W measured with a power meter (Thorlabs PM100D) with 95% accuracy. To compute the responsivity, we need to determine the equivalent current response generated by the QPD. This can be achieved by using the measured $V_{\mathrm{RMS}}$ values and the known transimpedance (r), as described by the equation:

$$I = \frac{V_{\mathrm{RMS}}}{r} \tag{5.6}$$

where $V_{\mathrm{RMS}}$ is in volts (V) and $r$ is in ohms ($\Omega$), and current $I$ in amperes (A). A plot showcasing one of the output channels (sum) of the initial QPD measurements, with the y-axis converted to units of amperes (A), is illustrated in figure 5.18. We calculate the mean of the data points shown in the plot and determine the responsivity (R) as follows:

$$R = \frac{0.0695\,\mathrm{mA}}{167\,\mu\mathrm{W}} = 0.415\,\mathrm{A\,W^{-1}}.$$

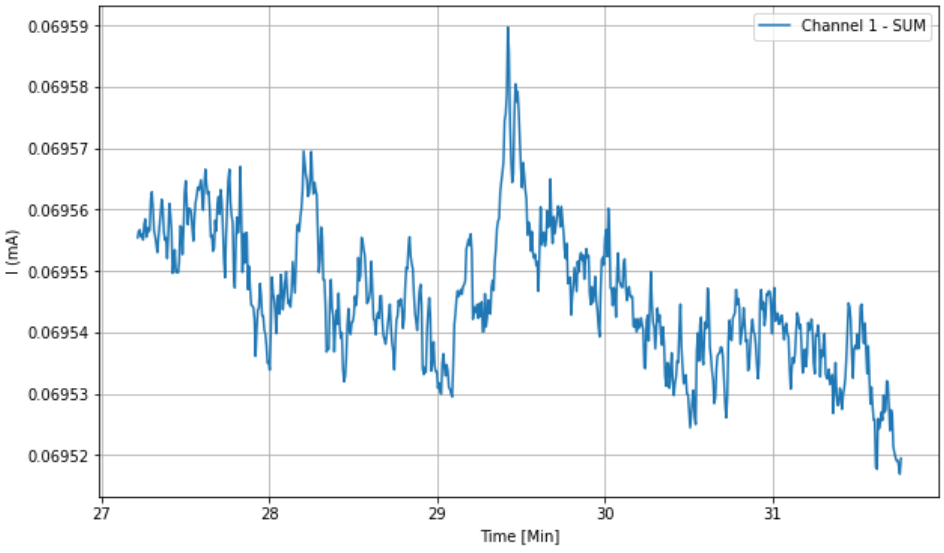


**Figure 5.18:** A stable part of one of the QPD measurements. The plot represents the output of the total sum (S) from all four quadrants of the QPD.

### Displacement Calibration Factor

The objective of conducting stability measurements is to quantify the spatial drifts of the beam in terms of units of length. Merely observing the changes in $V_{RMS}$ or I values does not provide sufficient information regarding these drifts. To achieve a more informative measure, a conversion factor from $V_{RMS}$ (in volts) to displacement (in meters) is necessary. This is accomplished by calculating the variation in power across the two halves of the QPD, using the previously defined responsivity.

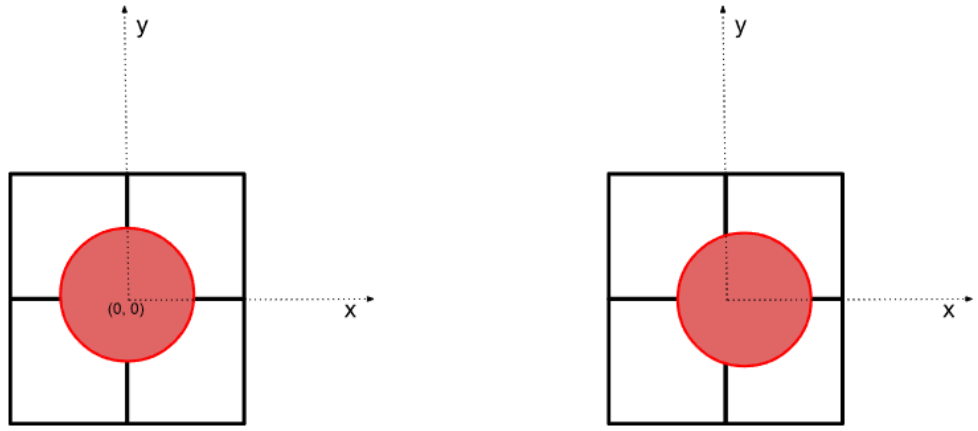


**(a)** Centered beam **(b)** Shifted beam

**Figure 5.19:** A schematic representing the laser beam spot on a QPD such that the center of the beam is at different location along the x-axis. There is no change in power in the two halves (vertical) of the QPD, separated by the x-axis.

Consider a scenario where a laser beam is precisely aligned at the center of a QPD, such that the light's intensity is evenly distributed across all four quadrants, as depicted in figure 5.19a. In subsequent analyses, the beam is assumed to have a radius (w) of 250 microns, with the beam power computed to be 167 $\mu$W. To simplify our calculations, we will consider that the displacement of the beam spot occurs solely along the x-axis of the transversal plane, as illustrated in figure 5.19b. This displacement results in a nonzero differential power between the two halves of the QPD. The first part of the problem is to quantify this change in power due to the beam's movement along the x-axis. Therefore, we characterize our laser beam with a function dependent only on x. The Gaussian intensity distribution of the beam is defined by the following equation:

$$I(x) = I_o e^{-2(x/w)^2} \tag{5.7}$$

where $I_o$ is the peak intensity at the center of the beam (x=0), and w denotes the beam radius. To determine the power of the beam, one can integrate the intensity distribution, which is expressed mathematically as:

$$P = \int_{-\infty}^{\infty} I_o e^{-2(x/w)^2}\, dx. \tag{5.8}$$

Note that although our beam has a finite size, we take the integral limits from $-\infty$ to $+\infty$ for simplicity. This approach is taken because integrating the Gaussian function over an infinite domain simplifies calculations, resulting in an expression involving the error function. Additionally, the beam's intensity decreases significantly at radial distances much larger than the beam size.

The formula presented in equation 5.8 calculates the total power of our beam. This equation is akin to Gaussian integrals, characterized by:

$$\int_{-\infty}^{\infty} e^{-at^2}\, dt$$

and which are directly related to the error function (erf) and the complementary error function (erfc). The error functions are defined as follows:

$$\text{erf}(x) = \frac{2}{\sqrt{\pi}} \int_0^x e^{-t^2}\, dt, \tag{5.9a}$$

$$\text{erfc}(x) = 1 - \text{erf}(x) = \frac{2}{\sqrt{\pi}} \int_x^\infty e^{-t^2}\, dt. \tag{5.9b}$$

Returning to the discussion on the distribution of the beam on a QPD, when the beam is precisely centered, the power distribution is equal, with each half of the QPD receiving 50% (83.5 $\mu$W) of the total power. This symmetry enables the calculation of power on one half of the QPD by integrating the intensity profile over half of its area. A spatial drift results in a nonzero differential power between the two halves. For the purposes of our calculations, we will assume a spatial displacement of the beam to be 10% of the beam radius, i.e., 25 microns, along the x-axis only. Considering the symmetric nature of the beam and a shift of 25 microns, the power in the right half of the QPD (as shown in figure 5.19b) is given by:

$$P_{25} = \int_0^\infty I_o e^{-2\left(\frac{x-25}{w}\right)^2}, dx \tag{5.10}$$

To link equation 5.10 with the error function, we introduce the following substitution:

$$u = \frac{\sqrt{2}(x - x_o)}{w}$$

accompanied by a change of the differential:

$$dx = \frac{w du}{\sqrt{2}}$$

where $x_o$ = 25 microns, represents the displacement of the beam's center from the origin. Implementing this substitution, equation 5.10 is transformed to:

$$P_{25} = \frac{I_o w}{\sqrt{2}} \int_{-25\sqrt{2}/w}^\infty e^{-u^2} du. \tag{5.11}$$

The integral in this equation is effectively represented by the complementary error function:

$$P_{25} = \frac{I_o w \sqrt{\pi}}{2\sqrt{2}} \text{erfc}\left(-\frac{25\sqrt{2}}{w}\right). \tag{5.12}$$

The coefficient preceding the error function represents the total power of the beam. This assertion can be validated by integrating equation 5.8 and applying the outcomes of Gaussian integrals. The inclusion of the factor 2 stems from our focus on obtaining only half of the beam's power. Consequently, the power on the right half of the QPD is articulated as:

$$P_{25} = \frac{P_o}{2} \text{erfc}\left(-\frac{25\sqrt{2}}{w}\right). \tag{5.13}$$

This expression captures how the power distribution on right half of the QPD can be quantified, incorporating the beam's displacement through the use of the complementary error function.

The aforementioned construct indicates that a shift of 25 microns results in an increase of power in the right half by 13.2 $\mu$W. The responsivity (R) of the QPD is used to compute the differential current, $\Delta I$, resulting from the power change.

$$\Delta I = 2(0.41\,\text{A/W} \times 13.23\,\mu\text{W}) = 0.01\,\text{mA}.$$

Considering the transimpedance (10 V/mA), the differential voltage is computed to be $\Delta V_{\text{RMS}} = 0.1$ V. From this, the conversion factor, which is essential for translating voltage changes into beam spatial movement, is derived as:

$$C = \frac{0.1}{25} = 4\,(\text{mV}/\mu\text{m})$$

The following discussions and results will use this conversion factor to translate the output of the QPD amplifier (in $V_{RMS}$) into beam spatial displacement in units of length.

### Stability Results

Laser stability measurements were conducted at five different positions prior to the PC setup. Among these, three measurements were well-calibrated, with the beam perfectly centered and its size (radius) converged to about 250-300 microns. This thesis will primarily focus on one of these measurements, performed after the telescope in the pre-conditioning setup of the laser beam. At this location, three 24-hour long measurements (M1, M2, and M3) were conducted. We will focus specifically on the quiet measurements, which were taken during periods of no activity in the lab. The external lab environment significantly impacts these sensitive measurements, particularly in terms of vibrational displacements, which are prominently observed in our stability assessments.

First, we will present the actual measurement results measured in $V_{RMS}$ for all channels: S, X, and Y. The corresponding plots for these channels are shown in figure 5.20. The X and Y channels have been normalized, meaning they have been divided by the total sum (S). Normalizing by the sum makes the results independent of power fluctuations, focusing instead on the relative differences in intensity among the quadrants. The difference in absolute values of these different measurements suggest sudden misalignments in the setup or an abrupt environmental change, such as a mechanical shock. After this sharp change, the signal appears to stabilize, suggesting that the cause of the disturbance has been resolved or that the system has adjusted to a new position.

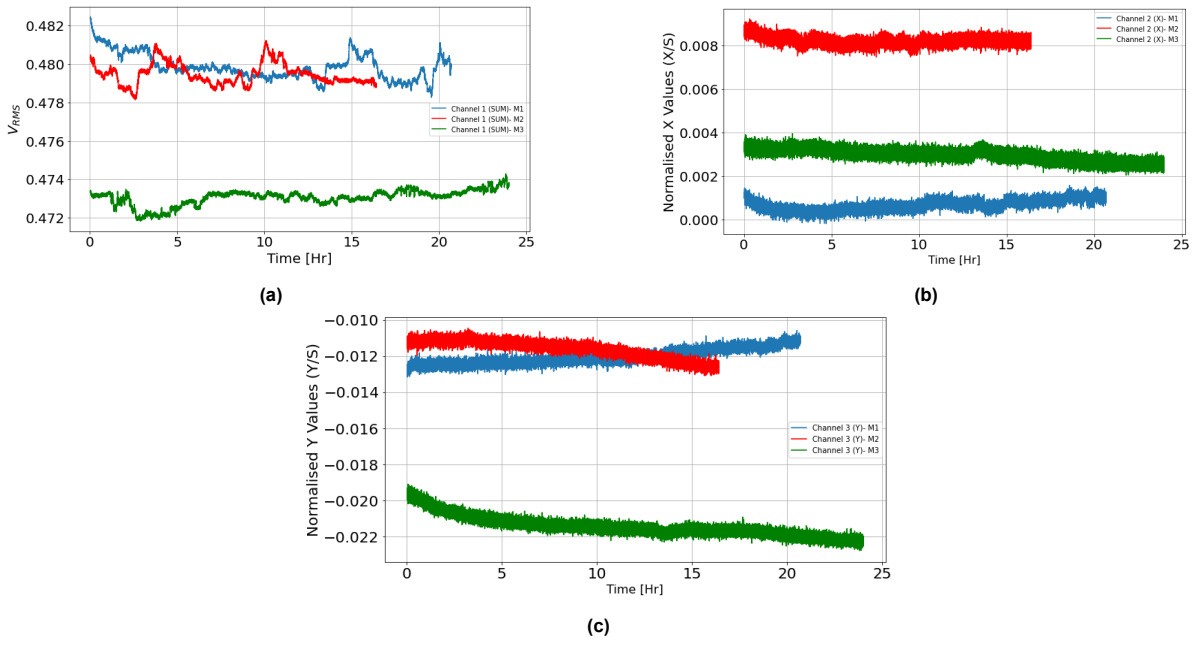


**Figure 5.20:** Results of all the three outputs of the QPD amplifier, measured in $V_{RMS}$, for three different measurement periods.

Figure 5.21 presents the beam displacement for measurement 3. The figure clearly indicate a directional movement of the laser beam. In the X direction, we observe the beam slightly drifting towards the right or center of the QPD, with a total drift of about 0.2 $\mu m$ over a 24-hour cycle. Similarly, in the Y direction, there is a total drift of approximately 0.45 $\mu m$, suggesting a consistent vertical displacement of the laser beam. Similar results are observed for other measurements. These displacements, although minor, could potentially become more significant over larger distances from the measurement position, if the displacement of the beam on the QPD is due to changes in the beam angle $\theta$, in accordance with the principle l = r$\theta$. This implies that the farther the measurement point from the laser, the more

pronounced these displacements may appear. The measurement results are consistent enough to suggest that the laser remains relatively stable, with minimal drift observed, at least in the 24 hour cycle. Therefore, it is unlikely that these slight movements alone are responsible for any major misalignments within the PC setup. Although it is plausible that these measurements of 3 $\times$ 24 hours are too short to capture long time-scale drifts, permanent monitoring of the beam might be required to detect these drifts.

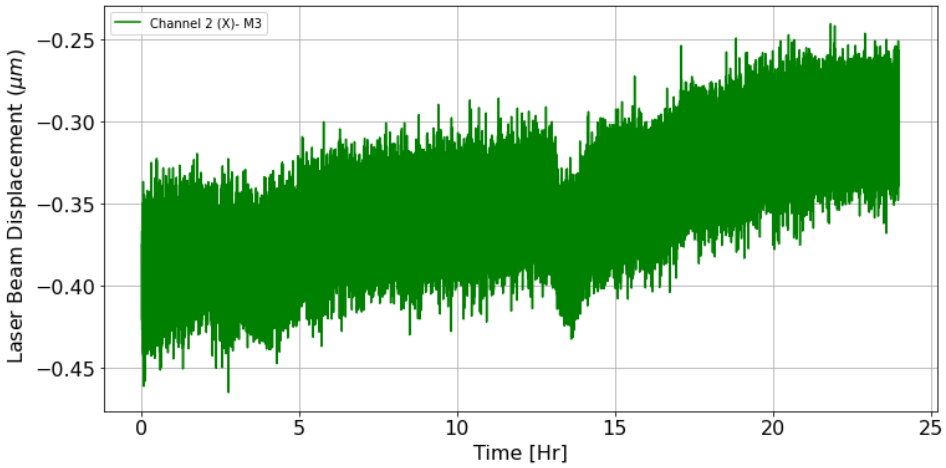


**(a)** Laser beam displacement for channel X of the QPD over 24 hour cycle.

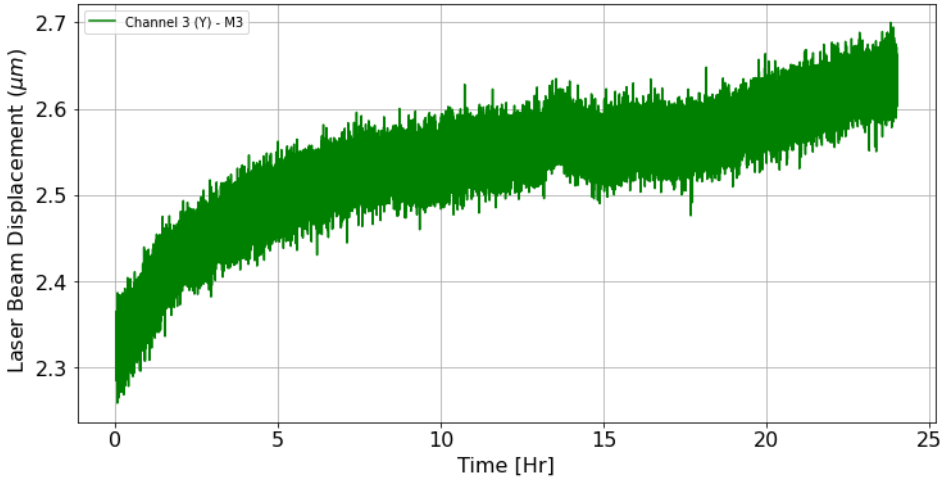


**(b)** Laser beam displacement for channel Y of the QPD over 24 hour cycle.

**Figure 5.21**

## 5.3. Phase Resolution

With all the stability measurements conducted, we identified several major noise sources that contribute to the drifts (fluctuations) in the setup and phase measurements. As mentioned at the start of this chapter, we performed phase measurements at various times throughout this research. These measurements were part of our experimental efforts to optimize and improve phase resolution by identifying noise sources and isolating the setup from them. In this section, we will primarily discuss the phase resolution and the jitter (integrated phase noise) of most of the phase measurements performed in this work. We will also detail the changes made to the setup for these measurements. Towards the end of this section, we will compare the phase resolution of the PC from the initial to the final phase measurements and also with the phase measurements performed prior to this research (reference [6]).

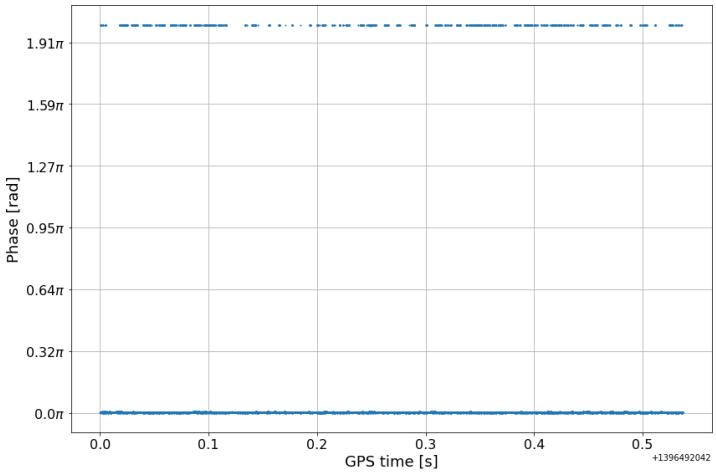


**Figure 5.22:** Corrupt single phase measurement frames which are excluded from the analysis.

To compute the phase resolution, we measured the standard deviations (resolution) for multiple intervals of the phase measurements at a given timestamp, as outlined in the introduction of this chapter. Any standard deviations that significantly deviated from the others were excluded. These deviations correspond to the anomalies in the phase measurements observed time to time. One such measurement is shown in figure 5.22. We can clearly see that this phase measurement differs greatly to other measurements shown in figure 5.2a-5.2d. To enhance the accuracy, we combined all the resolution calculations and computed the weighted average $\sigma_{avg}$ using the following formula [6]:

$$\sigma_{\text{avg}} = \sqrt{\frac{\sum_{i=1}^{k}(n_i - 1)\sigma_i^2}{\sum_{i=1}^{k} n_i - k}}$$

where k is the number of intervals which is 100 for all our measurements, and $\sigma_i$ and $n_i$ represent the standard deviation and the sample size of the individual intervals, respectively. To maintain uniformity, the sample size was set at 6000, which corresponds to about 200 ms of recorded phase measurements. We also relate the phase resolution to the optical path length fluctuations of the two beams using equation 5.3, under the paraxial wave approximation. To compute the jitter (integrated phase noise) for our measurement in a given timestamp, we calculate the mean of the individual jitter values obtained from 100 single measurements. The cut-off frequency for the jitter calculations is 10 Hz. A summary of all the phase measurements performed, along with their measured phase resolution and jitter, is presented in table 5.1. The table also details the major structural changes associated with these measurements, providing an overview of the adjustments made to enhance measurement accuracy and stability.

From the table, it is evident that the initial phase resolution of the system exceeded 20 mrad for all measurements. A significant enhancement in resolution was achieved when the scanner, which exhibited a broadband resonance frequency at frequencies between 2.3-2.7 kHz and above 3.2 kHz, was replaced with a plane mirror. The measured jitter for the fourth measurement (GPS timestamp: 1388398000), as shown in the table, in the frequency range of 2.2-4.5 kHz, is about 9.5 mrad. The observed improvement in total resolution after the removal of the scanner is approximately 10.3 mrad, indicating compatible results. Further refinements to the setup, including suspending the optical bench, allowed us to achieve a phase resolution of about 5.2 mrad in our final measurements.

The phase noise PSD of the initial, intermediate, and final measurements is displayed in figure 5.23. From this plot, it is clear that the phase noise floor of the PC setup has significantly improved. The remaining noise primarily stems from the resonance of the optical mounts and components, particularly noted between 200-700 Hz. There is also some acoustic noise present in the PSD, but it has comparatively lower power. The removal of the scanner substantially reduced the noise floor for higher frequencies, especially beyond 1500-2000 Hz. Additionally, suspending the bench has mitigated the effects of low-frequency disturbances such as airflow, enhancing the stability of the setup. Overall, these

**Table 5.1:** Summary of the Phase Measurements

| Timestamp (GPS) | Phase Resolution (mrad) | OPD (nm) | Jitter (mrad) | Structural Changes |
|---|---|---|---|---|
| 1386554000 | 20.4 | 3.46 | $21.1 \pm 0.6$ | N/A |
| 1386697000 | 24.5 | 4.15 | $25.1 \pm 0.4$ | N/A |
| 1387107800 | 25.7 | 4.36 | $25.1 \pm 0.5$ | N/A |
| 1388398000 | 15.2 | 2.57 | $13.3 \pm 0.4$ | Improved reference signal power, alignment at the scanner, and polarisation of the beam. |
| 1393550000 | 16.5 | 2.8 | $13.6 \pm 0.5$ | N/A |
| 1395597000 | 6.2 | 1.05 | $6.1 \pm 0.4$ | Scanner was removed |
| 1395970000 | 5.7 | 0.98 | $5.6 \pm 0.5$ | Alignment correction |
| 1396492000 | 5.25 | 0.89 | $5.1 \pm 0.4$ | Suspension of the optical bench |

adjustments have improved the phase resolution of the system by a factor of 4-5 times compared to the starting condition, with a significant reduction in the phase noise floor, demonstrating improvement in measurement accuracy and stability.

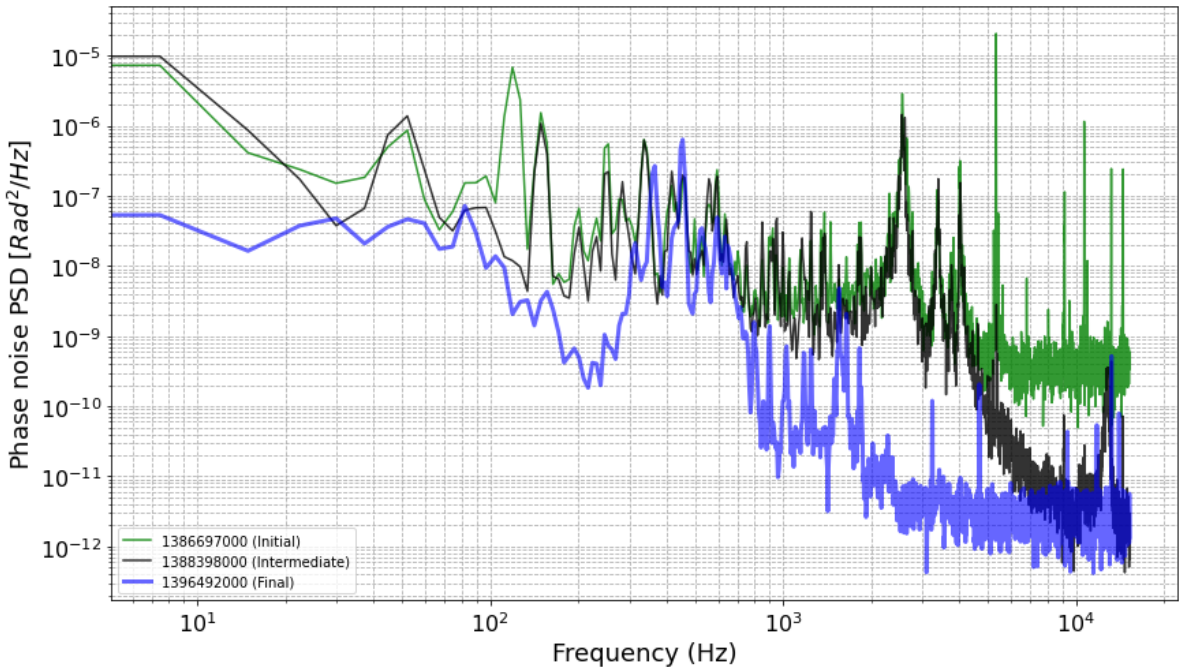


**Figure 5.23:** A comparative study of the phase noise power spectral density of different measurements performed at various stages throughout this research.

Overall, the initial measured phase resolution of the setup was about 25 mrad, which corresponds to an optical path length differences (OPD) of approximately 4.2 nm ($\sim \lambda/250$ at $\lambda$ = 1064 nm). With improvements made to the setup, we were able to enhance the phase resolution to approximately $\sim \lambda/1200$. The required phase resolution for the PC is about 12 mrad (< $\lambda$ / 500), which corresponds to optical path length differences of about 2 nm. Based on the results of the final phase measurements, we are well within the required phase resolution but without the scanner. The limit of the phase resolving capabilities of the PC is unknown, which suggests potential for further improvement. This can be particularly achieved by mitigating the effects of vibrations in the 200-700 Hz range that is observed

for the mounts and optical components. The jitter contribution from these vibration peaks observed in our final measurements corresponds to about 4.8 mrad. By removing this vibrational noise, we could further improve the phase resolution to 0.3 - 0.4 mrad ($\lambda/3200$) approximately. Achieving this resolution would mean that most of the dominant phase noise sources would be effectively eliminated from the PC setup. What would remain are the acoustic noise sources; however, as observed from the phase measurements, these do not significantly affect the phase resolution of our setup.

### 5.3.1. Comparison with Previous Measurements

The PSD of the very initial and final phase measurements performed in this research is plotted alongside the phase measurement from prior work in figure 5.24. The measured phase resolution in the previous study was approximately 7.1 mrad [6].

From the plot, it is evident that the phase noise at the start of our measurements was exceptionally high compared to both the final and previous measurements. The starting (initial) measurements resulted in poor resolution, primarily due to low-frequency noise sources in the 0-200 Hz range and amplification of other noise sources beyond 200 Hz. Notably, there is some resonance observed at 2.3-2.7 kHz and 3 kHz in the previous measurement as well, with the only difference being that the power at these frequencies was relatively low. These peaks definitely correspond to the scanner itself. In all the three measurements exemplified, we observed broadband resonances in the 200-700 Hz range. Based on these observations, it seems that the overall noise floor of the setup increased (or amplified) significantly between the previous work and the current work. This overall increase in the noise floor led to poor measured phase resolution.

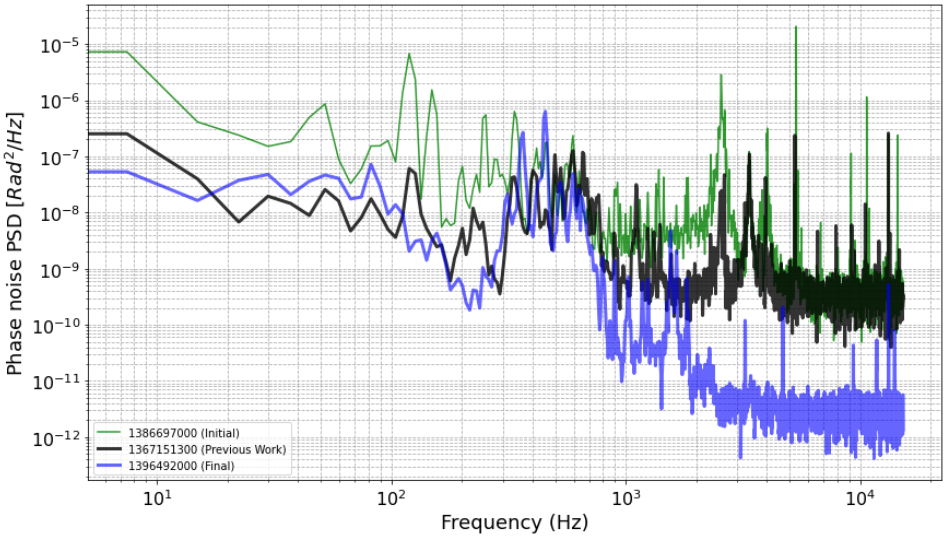


**Figure 5.24:** Comparative study of phase noise PSD, showing measurements from this study alongside measurement from previous work.

# 6

# Summary & Conclusion

In this work we first characterized the PC interferometer setup to assess its operational accuracy and ensure it meets its design criteria. We studied the nature and properties of our laser beam and also compared these measurements with ideal beam propagation computed using the ABCD law. We conducted independent studies on the beam characteristics in the two arms of the interferometer. The profiling results show that both beams exhibit a well-defined Gaussian profile ($TEM_{00}$), with slight astigmatism observed in their structure. The ellipticity, which indicates the level of astigmatism, is close to 1 for the reference beam, suggesting minimal astigmatism. In contrast, the test beam, particularly post-EOM, shows higher levels of astigmatism with ellipticity values below 0.87. Overall, the beam quality and shape are consistent with the design. They are well-scaled to the optics used and collimated where necessary. This characterization study confirms the reliability of the overall PC prototype design and its operational accuracy.

To better understand the phase measurement capabilities of the PC setup, we performed static relative phase measurements of the heterodyne beat signal (80 MHz), without probing the phase modulated (sideband) frequencies of the laser beam wavefronts. In the initial phase measurements, we observed significant fluctuations, especially in the small time-scales of the measurement $\simeq$ 200 ms. The measured resolution of the system was approximately 25 mrad. These fluctuations were primarily due to drifts in the setup. To determine the sources of phase noise, we conducted a range of stability measurements – vibrational, acoustic, seismic, and laser stability.

With the stability measurements, we identified several noise sources that contribute to poor phase resolution. The primary sources were vibrational and acoustic. The optical mounts and components of the setup each resonate at their unique frequencies, particularly within the 200-700 Hz frequency range. The scanner exhibits resonances at 2.3-2.7 kHz and 3.3 kHz, with phase noise density in the order of a few $10^{-6}$ $rad^2/Hz$. These resonances are broadband, hence they contribute significantly to overall phase noise. Other dominant noise sources are primarily acoustic, particularly noted at 83 Hz, 1.25 kHz, and 3 kHz. The 83 Hz acoustic noise causes the optical bench to resonate vertically at this frequency.

To enhance the phase resolution, we removed the scanner and replaced it with a mirror, and suspended the optical bench. This modification resulted in a measured phase resolution of approximately 5.3 mrad ($\sim \lambda/1200$), showing decent improvement. By removing the scanner, the overall noise floor of the setup significantly decreased, especially for frequencies above 1000 Hz. The remaining dominant noise sources are now the resonances of the optical mounts, primarily within the 200-700 Hz range. Through these various experimental endeavors, we identified several major noise sources and improved the resolution of the PC setup by a factor of 4-5 times compared to its initial condition.

Overall the PC setup is very stable and the measured phase resolution, without the scanner, is well within the requirements. If we are able to remove these remaining resonances of the mounts, it

is expected that we will be able to measure the phase with a resolution less than 0.5 mrad. Achieving this resolution will significantly improve the reliability and stability of the phase measurements.

## 6.1. Future Work

Since the scanner is crucial for achieving the scientific goals of the PC, future research should explore the dynamics and resonances of the scanner mount. Developing damping methods could help minimize the impact of these resonances. Additionally, understanding the resonances of individual mounts and optical components could further improve resolution.

Furthermore, additional studies are necessary to definitively determine the nature of the beam in our setup, whether it is simple astigmatic or general astigmatic. In this work, we have assumed the beam to be simple astigmatic, but the angle changes observed from the beam profiling measurements suggest that the beam might be general astigmatic. In terms of modelling and performing simulations, it would be ideal to know the true nature of the beams (and wavefronts) in our setup.

Another significant aspect is the continuous monitoring of the laser beam to detect any long-term drifts. This could be achieved by splitting the beam before it enters the setup and calibrating a QPD to enable monitoring. It is also crucial to understand the challenges associated with using optical fibers. The 2-meter length of the fiber adds a significant amount of OPL to the reference beam. Matching the OPL of the two arms is essential to ensure temporal coherence and eliminate the effects of unequal path lengths on the measured phase resolution.

# Bibliography


[1] LIGO Caltech. *LIGO*. https://www.ligo.caltech.edu/page/why-detect-gw. Accessed: 2024-03-20.

[2] L. van der Schaaf. “The Phase Cameras of Advanced Virgo”. English. PhD-Thesis - Research and graduation internal. Vrije Universiteit Amsterdam, 2020. ISBN: 9789402818642.

[3] Charlotte Bond et al. “Interferometer techniques for gravitational-wave detection”. In: *Living reviews in relativity* 19 (2016), pp. 1–217.

[4] Kazuhiro Agatsuma et al. “High-performance phase camera as a frequency selective laser wavefront sensor for gravitational wave detectors”. In: *Optics express* 27.13 (2019), pp. 18533–18548.

[5] Kazuhiro Agatsuma et al. “Phase camera experiment for Advanced Virgo”. In: *Nuclear Instruments and Methods in Physics Research Section A: Accelerators, Spectrometers, Detectors and Associated Equipment* 824 (2016), pp. 598–599.

[6] Friso J. Hoogenberg. *Characterization of a phase camera for the Virgo gravitational wave detector*. Accessed: 2024-02-05. 2023. URL: https://repository.tudelft.nl/islandora/object/uuid:28296973-bfbf-4df2-85ab-67eb272e1a7e?collection=education.

[7] Justin Peatross and Michael Ware. “Physics of light and optics: a free online textbook”. In: *Frontiers in Optics*. Optica Publishing Group. 2010, JWA64.

[8] Bahaa EA Saleh and Malvin Carl Teich. *Fundamentals of photonics*. john Wiley & sons, 2019.

[9] Eugene Hecht. *Optics*. Pearson Education India, 2012.

[10] Javier Alda. “Laser and Gaussian beam propagation and transformation”. In: *Encyclopedia of optical engineering* 999 (2003), pp. 1013–1013.

[11] Michael Kovalev et al. “Reconstructing the spatial parameters of a laser beam using the transport-of-intensity equation”. In: *Sensors* 22.5 (2022), p. 1765.

[12] Dipl.-Math Evgenia Kochkina. *Stigmatic and Astigmatic Gaussian Beams in Fundamental Mode-Impact of Beam Model Choice on Interferometric Pathlength Signal Estimates*.

[13] Jacques A Arnaud and Herwig Kogelnik. “Gaussian light beams with general astigmatism”. In: *Applied optics* 8.8 (1969), pp. 1687–1693.

[14] Keisuke Goda et al. “Frequency-resolving spatiotemporal wave-front sensor”. In: *Optics letters* 29.13 (2004), pp. 1452–1454.

[15] Stephen M Anthony and Steve Granick. “Image analysis with rapid and accurate two-dimensional Gaussian fitting”. In: *Langmuir* 25.14 (2009), pp. 8152–8160.

[16] *Gaussian2dModel — Non-Linear Least-Squares Minimization and Curve-Fitting for Python*. 2024. URL: https://lmfit.github.io/lmfit-py/builtin_models.html#lmfit.models.Gaussian2dModel (visited on 10/01/2023).

[17] Wikipedia. *Gaussian function — Wikipedia, The Free Encyclopedia*. [Online; accessed 8-March-2024]. 2024. URL: https://en.wikipedia.org/wiki/Gaussian_function.

[18] Astropy Collaboration. *Gaussian2D — Astropy v5.1.dev2283+gc16a8e04d*. [Online; accessed 8-March-2024]. 2024. URL: https://docs.astropy.org/en/stable/api/astropy.modeling.functional_models.Gaussian2D.html.

[19] Mephisto. *Ultra-Narrow Linewidth CW DPSS Laser*. https://www.coherent.com/resources/datasheet/lasers/mephisto-mephisto-s-ds.pdf. Accessed: 2024-05-02.

[20] Herbert Gross. “Handbook of Optical Systems”. In: (2005).

[21] Peter J De Groot. “Vibration in phase-shifting interferometry”. In: *JOSA A* 12.2 (1995), pp. 354–365.

[22] Chien-ming Wu and Ching-shen Su. “Nonlinearity in measurements of length by optical interferometry”. In: *Measurement Science and Technology* 7.1 (1996), p. 62.

[23] Vinzenz Wand et al. “Noise sources in the LTP heterodyne interferometer”. In: *Classical and Quantum Gravity* 23.8 (2006), S159.

[24] Yanqi Zhang et al. “Investigation and mitigation of noise contributions in a compact heterodyne interferometer”. In: *Sensors* 21.17 (2021), p. 5788.

[25] Gerhard Heinzel et al. “Investigation of noise sources in the LTP interferometer S2-AEI-TN-3028”. In: (2008).

[26] Kimmo Kokkonen and Matti Kaivola. “Scanning heterodyne laser interferometer for phase-sensitive absolute-amplitude measurements of surface vibrations”. In: *Applied Physics Letters* 92.6 (2008).

[27] Philip Koch. “Design, suspension and optical characterization of the beam splitter and output mode cleaner for the AEI 10 m prototype”. In: (2022).

[28] Newport. *Design Consideration for Opto-Mechanics Part 1*. https://www.newport.com/medias/sys_master/images/images/he8/hbf/8983778852894/MI-011603-White-Paper-web-Partner-Ad.pdf. Accessed: 2024-03-20. 2023.

[29] *GNA-190 QUADRANT PD AMPLIFIER T4*. https://wiki.nikhef.nl/gravwav/images/5/57/Gna190.pdf. Accessed: 2024-03-20.

[30] Hamamatsu. *Si PIN Photodiodes*. https://www.hamamatsu.com/content/dam/hamamatsu-photonics/sites/documents/99_SALES_LIBRARY/ssd/s5980_etc_kpin1012e.pdf. Accessed: 2024-03-20.